remote sensing

MDPI

Article

Integration of Multispectral and Hyperspectral Satellite Imagery for Mineral Mapping of Bauxite Mining Wastes in Amphissa Region, Greece

Evlampia Kouzeli [1], Ioannis Pantelidis [2], Konstantinos G. Nikolakopoulos [1,*], Harilaos Tsikos [2] and Olga Sykioti [3]

[1] GIS and Remote Sensing Lab, Department of Geology, University of Patras, 26504 Patras, Greece; e.kouzeli@upatras.gr
[2] Department of Geology, University of Patras, 26504 Patras, Greece; geo14136@ac.upatras.gr (I.P.); htsikos@upatras.gr (H.T.)
[3] National Observatory of Athens, Institute for Astronomy, Astrophysics, Space Applications and Remote Sensing, 15236 Athens, Greece; sykioti@noa.gr
* Correspondence: knikolakop@upatras.gr

Highlights

What are the main findings?

- Spectral imagery overtakes spatial resolution, affecting results in mineral detection and discrimination.
- The main minerals like hematite and calcite are successfully mapped. The accessory phase minerals should be approached with caution.

What are the implications of the main findings?

- Remote sensing can provide valuable novel, accurate, fast, and cost-effective information on mineral mapping of bauxite mining wastes.
- Highlight potential gaps in identifying these minerals.

Abstract

The mineral-mapping capability of three spaceborne sensors with different spatial and spectral resolutions, the Environmental Mapping and Analysis Program (EnMap), Sentinel-2, and World View-3 (WV3), is assessed regarding bauxite mining wastes in Amphissa, Greece, with validation based on ground samples. We applied the well-established Linear Spectral Unmixing (LSU) and Spectral Angle Mapping (SAM) classification techniques utilizing endmembers of two established spectral libraries and incorporated ground data through geochemical and mineralogical analyses, X-ray fluorescence (XRF), Laser Ablation Inductively Coupled Plasma Mass Spectrometry (LA-ICP-MS), and X-ray Diffraction (XRD), to assess classification performance. The main lithologies in this area are bauxites and limestones; therefore, aluminum oxyhydroxides, calcite, and iron oxide minerals were the dominant phases as indicated by the XRF/XRD results. Almost all target minerals were mapped with the three sensors and both methods. The performance of EnMap is affected by its coarser spatial resolution despite its higher spectral resolution using these methods. Sentinel-2 is most effective for mapping iron-bearing minerals, particularly hematite, due to its higher spatial resolution and the presence of diagnostic iron oxide absorption features in the VNIR. World View 3 Shortwave Infrared (WV3-SWIR) performs better when mapping calcite, benefiting from its eight SWIR spectral bands and very high spatial resolution (3.7 m). Hematite and calcite yield the highest accuracy, especially with SAM, indicating 0.80 for Sentinel-2 (10 m) for hematite and 0.87 for WV3-SWIR (3.7 m) for calcite. AlOOH

Check for updates

Academic Editors: Joana Cardoso-Fernandes, Ana Cláudia Teodoro and Alexandre Lima

Received: 27 November 2025
Revised: 7 January 2026
Accepted: 15 January 2026
Published: 20 January 2026

Copyright: © 2026 by the authors. Licensee MDPI, Basel, Switzerland. This article is an open access article distributed under the terms and conditions of the Creative Commons Attribution (CC BY) license.

shows higher accuracy with SAM, ranging from 0.57 to 0.80 across the sensors, while LSU shows lower accuracy, ranging from 0.20 to 0.73 across the sensors. This study showcases each sensor's ability to map minerals while also demonstrating that spectral coverage and the spatial and spectral resolution, as well as the characteristics of the selected endmembers, exert a critical influence on the accuracy of mineral mapping in mine waste.

Keywords: bauxites; Multisensor Data; Spectral Angle Mapper; linear spectral unmixing; in situ data

1. Introduction

Bauxite is a rock type of sedimentary/residual origin and constitutes the primary ore of aluminum. It is used in a wide range of industrial applications such as aluminum production, refractories, and chemical products. The hydrated minerals gibbsite, boehmite, and diaspore along with goethite and hematite, kaolinite, and anatase constitute the majority of bauxite ores [1]. Like all ore resources, bauxite mining produces wastes that are exposed to the environment and potentially contain reactive material that could lead to the deterioration of the environment, possibly through air, water, and soil contamination.

The mapping of such mine waste is essential for sustainable mine site management and the protection of the environment. Satellite, airborne, and ground-based sensors are extensively used to assess and map mine waste and their associated mineralogical composition at both regional and site-specific scales across the world. Moreover, a growing interest in mine waste characterization (overburden, tailings, and residues) relates to potential raw material recovery [2].

In the context of multispectral data, ref. [3] suggests Advanced Spaceborne Thermal Emission and Reflection Radiometer (ASTER) and Sentinel-2 data for the mapping of hydrothermally altered areas in the rare, non-carbonated, and highly silicified listvenite rock at the Kaymaz Gold Deposit, Turkey. Meanwhile, ref. [4] utilizes Sentinel-2 imagery mapping in characterizing mine wastes of an Fe-Mn mine in Joda West, India. Similarly, ref. [5] adopts Landsat 8 OLI, ASTER, and Sentinel-2 in a long-term comparative study of Li-bearing mineral identification at the Bajoca, Feli, and Alberto mines in Spain and Portugal. Finally, ref. [6] employs ASTER satellite data at the Abu Marwat gold mine, Egypt, to detect hydrothermally altered minerals related to gold mineralization.

Under the framework of hyperspectral imagery, ref. [7] proposes Hyperion imagery to map iron oxide and clay minerals in the Tamera, Sidi Driss, and Boukhchiba mines in Tunisia. Earlier in a similar study, ref. [8] selected the Hyperion dataset and multiple methods to examine the capability of hyperspectral data to map iron ore distribution and correlate it with soil, water, and vegetation variables in the heterogeneous area of the Saranda Forest, Jharkhand, India, the location of the GUA Mine. Likewise, ref. [9] conducted mineralogical mapping at the Leviathan mine using AVIRIS, ProSpecTIR, and HyspIRI data, to investigate the acid mine drainage (AMD) pattern at different spatial and temporal scales. Elsewhere, ref. [2] maps bauxite mineral deposits in Saudi Arabia by targeting gibbsite as the most important mineral constituent of the ore using ASTER satellite data, thus highlighting ASTER's potential to investigate mineral resources.

More recent studies have employed a wide range of multispectral and hyperspectral satellite data processed using classical as well as more sophisticated classification techniques for mineral mapping. For example, Pléiades multispectral data were classified using the Maximum Likelihood algorithm to identify mining tailings in Mexico, achieving a success rate of over 80% [10]. Similarly, in bauxite mapping, ref. [2] classified ASTER data using the United States Geological Survey (USGS) spectral library.

Other researchers [2] compared multispectral Sentinel-2 imagery with hyperspectral PRISMA data for mapping bauxite mining residues in the Apulia region of Italy. Their results were validated through X-ray fluorescence (XRF) analysis and spectral measurements acquired using a laboratory spectroradiometer. In addition, PRISMA hyperspectral imagery has been used to detect alteration zones such as potassic, propylitic, and argillic zones, associated with a porphyry copper deposit in eastern Kazakhstan [11].

Sentinel-2 imagery was used to detect pegmatites and associated alteration zones in the Muiane and Naipa regions by applying various techniques, including RGB band combinations and ratios, principal component analysis (PCA), and supervised classification using Support Vector Machine and Maximum Likelihood algorithms [12]. Validation was carried out on field-collected samples using an ASD FieldSpec 4 spectrometer (Andover, MA, USA).

ASTER and Landsat 8 OLI multispectral imagery was processed using a novel unsupervised deep learning algorithm, namely a hybrid Variational Autoencoder, to detect and map argillic, silicic, phyllic, propylitic, and iron oxide alteration zones [13]. The validity of the identified targets was confirmed through field investigations and laboratory analyses, including XRF, spectroscopic, and microscopic techniques.

World View 3 (WV3) multispectral data were processed using the Spectral Angle Mapper (SAM) algorithm to map exposed bedrock and mine waste piles associated with legacy open-pit mining of sandstone-hosted roll-front uranium deposits along the South Texas Coastal Plain. At least 117 mine and mine waste-related features, most of which were previously unknown, were identified [14].

ASTER multispectral data were integrated with multiple machine learning algorithms for lithological mapping in southern Iran, including Random Forest, Support Vector Machine, Gradient Boosting, Extreme Gradient Boosting, and a deep learning artificial neural network [15].

Environmental Mapping and Analysis Program (EnMap) hyperspectral data were analyzed using heterogeneous ensemble learning methods, including bagging, boosting, stacking, voting, weighting, and blending, to overcome the challenges in the accuracy of hyperspectral lithological mapping in the Ameln Valley shear zone, Morocco [16].

Three multispectral datasets, including ASTER, Landsat-8, and Sentinel-2, were processed using techniques such as band ratios, PCA, and SAM to map the spatial distribution of carbonate minerals, OH-bearing minerals, and iron oxide minerals in Morocco [17].

Multispectral (ASTER) and hyperspectral (Hyperion) imagery were evaluated for mapping ophiolitic sequences and identifying manganese mineralization in the Bela Ophiolite region, Pakistan. Classical image processing techniques, such as band ratios, PCA, and SAM, were applied. Petrographic and geochemical analyses of in situ samples were conducted to cross-validate the classification results [18].

Sentinel-2 imagery was analyzed using the SAM algorithm to detect placer deposits on beaches in the Vigo Estuary, specifically at Limens and Santa Marta. Field samples were collected, and their spectral signatures were measured in the laboratory using an ASD FieldSpec 4 spectroradiometer [19].

With specific respect to lateritic deposits of Greece, ref. [1] proposes a novel method (linear Support Vector Machines) to discriminate Fe-Ni laterites from bauxites across outcrops, open pits, and stockpiles using Sentinel-2 satellite data. In a related study in Itea, ref. [20] uses linear unmixing to map bauxite mineral indicators using Sentinel-2 and WV3 satellite data. The same authors further demonstrate a new Laterite Spectral Index (LSI) to detect Fe-Ni laterite outcrops using Sentinel-2 data and compare its performance to other indices [14]. Meanwhile, ref. [21] maps aluminum concentrations in Greek bauxite residue using Sentinel-2 satellite data.

Moreover, SAM [6,8,22–25] and LSU [26–31] are among the most common methods used in analyzing satellite data: SAM calculates the spectral angle between the pixel and the endmembers [32], while LSU quantifies the fractional abundances of different endmembers within a mixed pixel [33].

All these recent studies demonstrate the strong potential of multispectral and hyperspectral remote sensing for mineral and mine waste mapping across diverse geological settings. However, despite methodological advances and increasing sensor availability, previous research has largely focused on individual datasets or algorithms. To date, no study has systematically evaluated the combined influence of spectral resolution, spatial resolution, and library endmember selection on bauxite mine waste mapping, validated against in situ mineralogy.

In this study, we focus on an abandoned underground bauxite mine, with particular focus given to mineral mapping of bauxite mining wastes. The innovation of this study lies in its first-time comparison of newly available hyperspectral EnMap data (30 m) with Sentinel-2 (10 m) and WorldView-3 Shortwave Infrared (WV3-SWIR; 3.7 m) data within a cross-sensor framework at different spatial resolutions. Additionally, the study integrates endmembers from two spectral libraries, the USGS [34] and Jet Propulsion Laboratory (JPL) [35], applies two spectral processing methods (SAM and LSU), establishes a common comparison framework to the EnMap 30 m spatial resolution by resampling Sentinel-2 and WV3-SWIR imagery to assess the effects of spectral and spatial resolution, and validates the results against ground data, including mineralogical identification of representative field samples using X-ray Diffraction (XRD) supported by bulk geochemical analyses (XRF and Laser Ablation Inductively Coupled Plasma Mass Spectrometry, LA-ICP-MS).

Using this methodology, the study points out the way in which the spectral coverage and spectral and spatial resolution affect the mineral mapping of mining wastes (referred to as "mine wastes" hereafter), how endmembers affect the results of each method, and how validation against ground data confirms the accuracy of the results, creating a benchmark for future mapping studies.

2. Materials and Methods

2.1. Geology

The study focuses on the inactive Arkoudotrypa bauxite mine in the Parnassos-Ghiona unit near Delphi, Central Greece (Figure 1). The area is characterized by preserved remnants of shallow-marine carbonate deposition of the Upper Jurassic to Tithonian–Cenomanian age. These carbonates form part of the extensive carbonate platform of the Parnassos-Ghiona unit, which developed from the Triassic to the Palaeocene in a shallow epicontinental sea bounded by the Pindos Ocean and the Pelagonian Belt, reaching thicknesses of up to ~1800 m [36]. The local paleoenvironment of deposition has been interpreted as neritic to reefal within the Subpelagonian–Pindos paleo-ocean [37,38], reflecting shallow-marine carbonate platform conditions with localized oolitic facies. Three episodes of subaerial exposure are recorded in the stratigraphy [39], preserved as distinct karst-type bauxite horizons of allochthonous origin, corresponding to the Callovian–Oxfordian, Kimmeridgian–Tithonian, and Cenomanian–Turonian intervals [40]. These short-lived emersion events caused freshwater alteration of the carbonate surfaces and subsequent karstification, creating mechanical traps where bauxitic material derived from the erosion of lateritic bauxites in the adjacent Pelagonian Belt was deposited as colluvium, talus, or fluvially reworked sediments [36,38,41,42]. These horizons are part of the Mediterranean bauxite belt [38,43,44] and are intercalated with their carbonate hosts. Mineralogical and geochemical evidence indicates that the formation of these lateritic bauxites occurred under tropical to subtropical

climates, predominantly at the expense of ophiolitic and associated lithologies, although remnants of the original lateritic crusts have not been observed in situ within Greece [38].

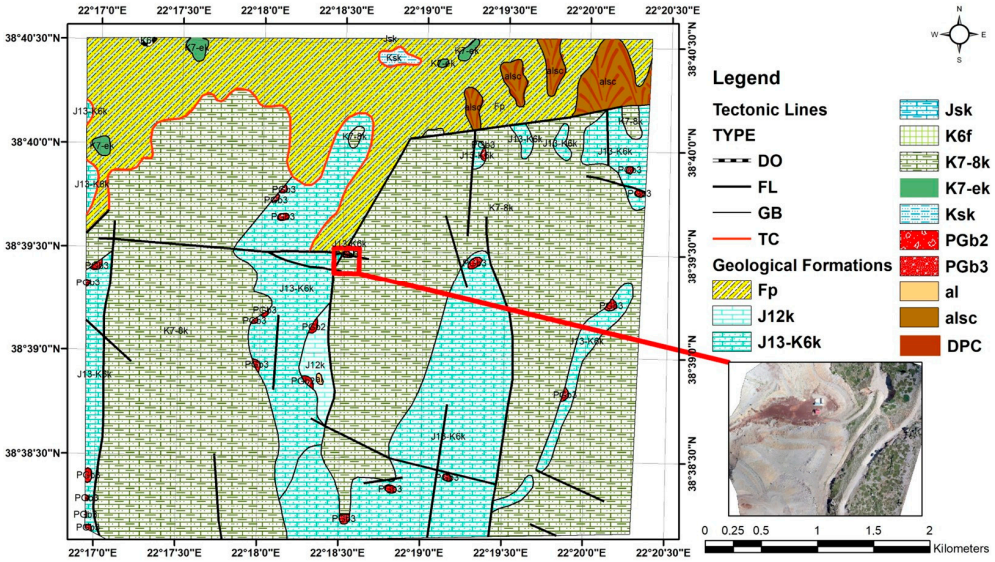


Figure 1. Study area: Inactive bauxite mine in the broader Delphi area, Central Greece. Geological map (Fp: undivided flysch, J12k: thick-bedded limestone, J13-k6k: undivided Upper Cretaceous milestones, Jsk: very karsty, compact dark colored limestone, K6f: Middle and Upper cretaceous formations (flysch-like rocks), K7-8k: compact or microcrystalline limestone, K7-ek: thin-bedded limestone, Ksk: Middle and Upper cretaceous formations (marl-plated limestone), PGb2: bauxite of the lower horizon, PGb3: bauxite of the upper horizon, DPC: talus and slope fan debris, al: recent alluvial deposits, and alsC: colluvial deposits).

The carbonate sequence hosting the bauxite horizons is composed of Triassic limestones and dolomites at its base, followed by thick Jurassic dolomitic limestones and dark oolitic limestones, and Tithonian strata, with Upper Cretaceous oolitic limestones marking the uppermost portion. Thin layers of pisolitic bauxite and bauxitic clay, defined as "satellite bauxite layers," occur locally in the uppermost carbonate beds [45]. The b3 horizon is capped in some locations by a thin coaly and carbonaceous facies, grading upward into organic matter-enriched limestone of the Turonian age, which is overlain by dark, homogenous calcilutites composed of wackestones and mudstones with ostracod and benthonic foraminiferal bioclasts [36,41].

Post-Cenomanian sedimentation transitioned to pelagic conditions in the Late Cretaceous, with deposition of thin Middle Campanian–Maastrichtian limestones [36,41,45]. Palaeogene clastic flysch sediments, up to 1500 m thick, followed unconformably, accompanied by Pliocene conglomerates and Quaternary deposits, reflecting ongoing tectonic activity and development of the Greek fold-and-thrust belts [46].

Overall, the Arkoudotrypa bauxite horizons illustrate the complex interplay of carbonate platform sedimentation, episodic karstification, lateritic weathering, and tropical to subtropical climate-driven bauxitization within a tectonically evolving region of the External Hellenides [38–40,46].

2.2. Satellite Data

EnMap and Sentinel-2 cover the visible to shortwave infrared spectral regions (400–2500 nm) whilst WV3-SWIR covers only the shortwave infrared spectral region. Atmospherically corrected EnMap data (acquired 19 June 2024) and VNIR-SWIR (224 spectral bands) data are provided by the Helmholtz Centre Potsdam, GFZ German Research Centre for Geosciences. The EnMap spectral bands 131–135 (1342.82–1390.48 nm) are affected

by water vapor absorption, giving too low reflectance values [47], and are thus excluded from further analysis. A Sentinel-2 Level 2A VNIR-SWIR image (12 spectral bands) is used [48], acquired on 26 June 2024. Finally, a dataset of WV3-SWIR (8 spectral bands) is also used (2024/01/06-SWIR). The WV3-SWIR data are atmospherically corrected by ReSe Applications. Furthermore, changing the signal-to-noise ratio (SNR) is not performed because (1) it is out of the scope of this study and (2) it can induce modifications in the initial reflectance values of the sensor. In total, five satellite datasets are employed to compare the results of mine waste mapping.

2.3. Spectral Libraries

The reference mineral spectral signature (referred to as "endmember" hereafter) from two different spectral libraries (reflectance values ranging from 0 to 1), namely the USGS and the JPL, is retrieved for the analysis of the satellite data. The USGS and JPL (Table 1 and Figure 2) endmembers of each of the six minerals pertinent to our site (diaspore, hematite, goethite, anatase, kaolinite, and calcite) are used with the SAM algorithm, revealing the endmembers with the lowest detected spectral angle threshold. Each mineral's endmember is used in the SAM analysis with EnMap, Sentinel-2, and WV3-SWIR data to identify which one results in the smallest spectral angle. Since the study area is characterized by fine-grained mineralogy, grain size is taken into consideration in conjunction with the spectral purity of the sample, as the spectral purity defines the presence/absence of contaminants. For this reason, all available endmembers of each mineral in each library are taken into consideration, corresponding to relatively pure samples with fine to medium grain size. In addition, based on the aforementioned criteria, the spectral signature of each mineral presenting the minimum detected spectral angle with each pixel spectrum is finally retained [49].

Table 1. A description of endmembers in this study. For each mineral in the second column, the first row corresponds to the spectral signature name in the United States Geological Survey (USGS) spectral library, and the second row corresponds to the spectral signature name in the Jet Propulsion Laboratory (JPL) spectral library. The spectrum title and information are retrieved from the corresponding ancillary file of each mineral from each spectral library [34,50,51].

Mineral	Spectrum Title
Diaspore	Diaspore_HS416.1B_ASDFRb Not Available
Hematite	Hematite_HS45.3_ASDFRb Hematite alpha Fe_2O_3 [oxide-none-medium-o01a]
Goethite	Goethite_HS36.3_BECKb Goethite alpha $Fe^{3+}O(OH)$ [hydroxide-none-fine-oh02a]
Anatase	Not Available Anatase TiO_2 [oxide-none-fine-o12a]
Kaolinite	Kaolinite_GDS11_lt63um_BECKb Kaolinite $Al_2Si_2O_5(OH)_4$ [silicate-phyllosilicate-fine-ps01a]
Calcite	Calcite_HS48.3B_BECKa Calcite $CaCO_3$ [carbonate-none-fine-c03a]

Moreover, the quartz endmember is not selected even if its presence is minor in the study area based on the laboratory results, since it is spectrally featureless in the VNIR-SWIR spectral area. Finally, we note that the diaspore spectrum is not available in the JPL spectral library, and the anatase spectrum is not available in the USGS spectral library. The boehmite spectral signature is not available in both the USGS and JPL libraries.

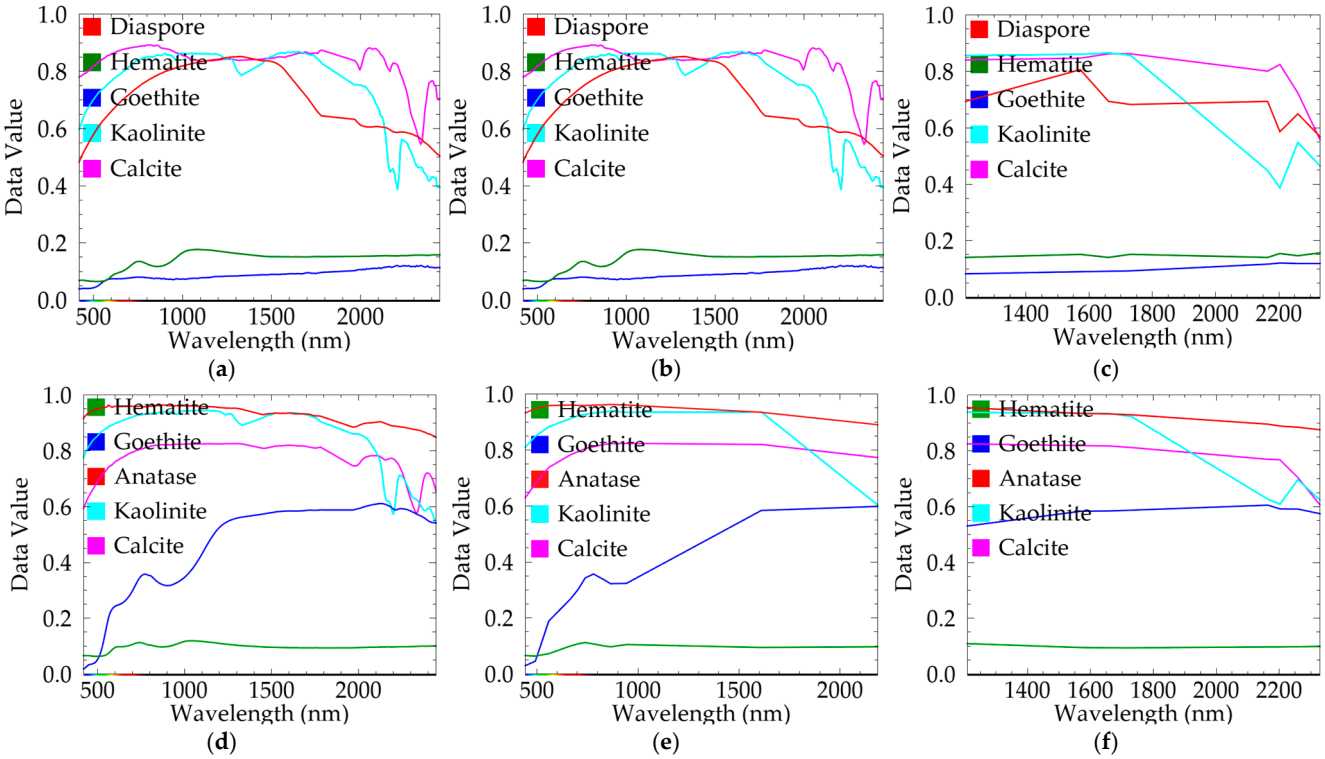


Figure 2. Mineral endmembers retrieved from the USGS spectral library and resampled to the (**a**) Environmental Mapping and Analysis Program (EnMap) spectral bands; (**b**) Sentinel-2 spectral bands; (**c**) and World View 3 Shortwave Infrared (WV3-SWIR) spectral band. Mineral endmembers in this study are retrieved from the JPL spectral library and are resampled to the (**d**) EnMap spectral bands; (**e**) Sentinel-2 spectral bands; (**f**) and WV3-SWIR spectral band.

2.4. In Situ Data

Ground samples are also collected, and laboratory analysis is conducted to validate the satellite results. A total of sixteen field samples of waste material (T) are collected from the abandoned Arkoudotrypa mine (Figure 1 and Table 2) in a 0.08 km^2 area. These represent poorly sorted, fragmentary mixtures of bauxite (B) and limestone (L) at variable modal proportions and particle sizes (generally sub mm- to cm-scale), with the limestone fraction being the modally most dominant in every instance. Care is taken to collect samples with particle sizes below 1.00 cm; representative larger fragments (4 bauxites and 13 limestones) are also collected and analyzed separately to aid material characterization.

Table 2. Quantitative XRF analysis (in wt%) of major oxide abundances in bauxites (B), limestones (A), and mixed waste samples (T) in study area (dashes indicate values below detection limit).

Sample Code	Al_2O_3	CaO	Fe_2O_3	K_2O	MgO	MnO	Na_2O	P_2O_5	SiO_2	TiO_2	L.O.I.
1B	46.68	0.15	18.32	0.45	0.37	0.06	0.08	0.04	17.48	2.00	11.26
1T	25.47	28.06	8.94	0.21	0.51	0.08	0.01	0.03	3.96	1.14	28.61
2B	37.25	0.22	36.19	0.47	0.49	0.05	-	0.08	6.51	1.72	12.05
2T	5.50	48.36	2.87	0.15	0.71	0.07	-	0.02	1.92	0.24	39.51
3B	50.47	0.13	18.59	0.30	0.35	0.09	0.05	0.04	13.35	2.18	11.54
3T	1.39	53.88	0.40	0.03	0.31	0.01	-	0.01	0.45	0.05	42.89
4T	1.10	53.95	0.25	0.07	0.59	0.01	0.01	0.01	0.92	0.04	42.81

Table 2. *Cont.*

Sample Code	Al_2O_3	CaO	Fe_2O_3	K_2O	MgO	MnO	Na_2O	P_2O_5	SiO_2	TiO_2	L.O.I.
5T	0.28	59.95	-	0.03	0.60	0.01	-	0.01	0.48	-	43.63
6T	1.10	58.17	0.15	0.08	0.66	0.02	-	0.01	0.81	0.04	43.02
7T	5.96	46.79	2.11	0.38	0.92	0.04	0.01	0.02	4.89	0.26	38.19
8T	0.61	54.24	-	0.09	0.55	0.01	-	0.01	0.99	0.02	43.10
9T	8.13	45.54	2.66	0.36	0.61	0.02	-	0.04	5.45	0.37	36.71
10B	54.01	0.15	15.71	0.91	0.56	0.04	0.06	0.06	9.98	2.38	11.71
10T	47.36	3.58	16.91	0.85	0.53	0.07	0.06	0.08	10.98	2.09	13.57
11T	11.24	43.31	4.05	0.22	0.80	0.04	-	0.03	3.83	0.51	36.17
12T	20.03	32.81	7.26	0.32	0.54	0.06	-	0.05	5.28	0.91	31.02
13T	11.26	40.91	5.36	0.42	0.81	0.07	-	0.05	5.97	0.50	34.82
14T	9.92	44.25	5.54	0.20	0.56	0.06	-	0.03	2.91	0.44	36.55
15T	16.10	37.52	6.26	0.27	0.62	0.05	-	0.03	4.27	0.70	33.23
16T	6.23	50.99	1.82	0.17	0.59	0.04	-	0.02	2.06	0.29	39.79
1-A	0.63	49.12	0.23	0.02	0.75	0.01	0.01	0.01	1.37	0.04	40.13
2-A	0.66	46.26	0.14	-	0.41	0.13	-	-	0.27	0.05	37.97
3-A	-	47.84	-	-	0.39	-	0.01	-	-	0.01	43.07
4-AA	0.96	49.05	0.33	0.01	0.65	0.01	0.01	0.01	1.64	0.05	39.74
4-AM	0.64	47.63	0.16	-	0.64	0.01	-	-	0.88	0.04	41.07
5-AA	3.33	45.14	2.44	0.01	1.20	0.01	0.01	0.01	5.07	0.12	38.97
5-AM	0.41	50.31	0.23	-	0.84	0.01	-	0.01	0.88	0.03	40.17
6-AAM	0.69	50.47	0.40	0.01	0.76	0.01	0.01	0.01	1.36	0.05	40.31
7-A	0.32	51.88	0.08	-	0.57	0.01	0.03	0.01	0.57	0.02	40.94
8-A	0.52	50.31	0.21	0.01	0.70	0.01	-	-	0.88	0.04	40.38
9-AAK	15.22	35.63	5.81	0.16	1.24	0.05	-	0.04	8.14	0.67	32.96
9-AMA	0.03	51.90	0.01	-	0.12	0.01	-	-	0.01	0.01	34.80
10-A	0.01	53.70	0.06	-	0.16	-	-	-	-	0.01	39.07

Analytical results are produced on finely ground samples via XRD for qualitative mineralogy and XRF for quantitative geochemical compositions and precise estimations of modal mineralogy. To further characterize the clay mineral fraction, separate experiments are conducted using thermal treatment at 490 °C for 2 h and ethylene glycol treatment at 65 °C overnight, allowing complementary ways to refine the XRD data and constrain as accurately as possible the clay mineral identification.

The bauxite mineralogy is dominated by aluminum oxyhydroxides (mainly boehmite and less diaspore), with hematite as a major additional constituent along with subordinate goethite. Accessory phases include TiO_2 polymorphs, kaolinite, and secondary vein calcite. The limestones consist chiefly of calcite but may contain variable amounts of additional dolomite along with minor clay minerals and quartz, likely representing diagenetic and detrital components, respectively [45]. Mixed waste samples naturally consist of combinations of the above minerals at variable modal proportions.

2.5. Methodology

The overall framework used in this study is shown in Figure 3. The methodology is divided into three key sections: data pre-processing, data processing, and output validation based on ground data. During pre-processing, the atmospherically corrected data are processed to have reflectance images, spectral libraries, and in situ data in the optimal format: reflectance values scaled to 0–1 [52], desired spatial resolution, and vegetation removal for the analysis. In the processing phase, mineral maps of the mining area are generated. Finally, in the validation phase, XRD results are used in conjunction with the resulting classification and abundance maps to assess the accuracy of the satellite-derived products. All data processing is carried out with ENVI 6.0 software.

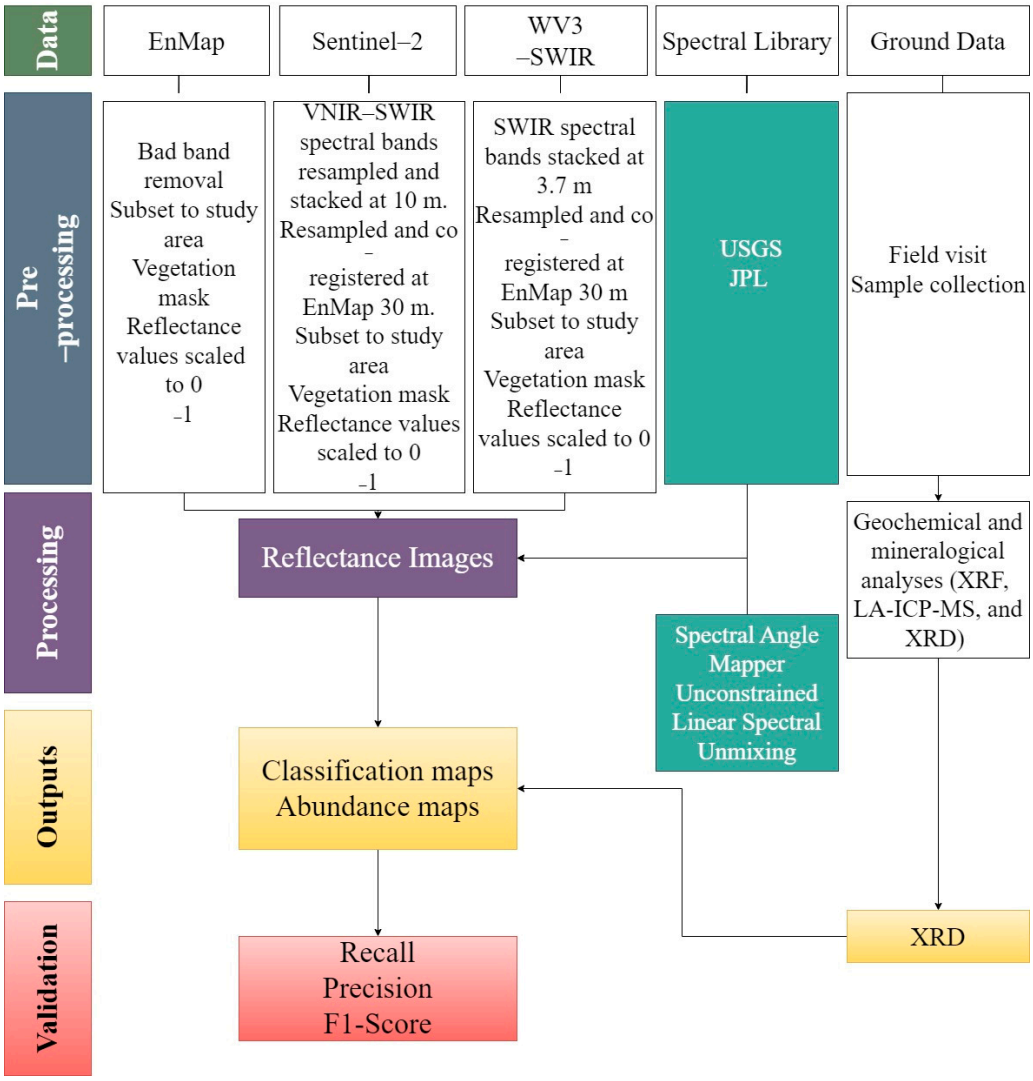


Figure 3. Methodology flowchart.

Five satellite datasets are generated for this study, with reflectance values ranging from 0 to 1: EnMap (30 m), Sentinel-2 (10 m and resampled to EnMap to 30 m), and WV3-SWIR (3.7 m and resampled to EnMap to 30 m). Sentinel-2 and WV3-SWIR satellite images are also resampled to 30 m spatial resolution and co-registered to EnMap to ensure spatial alignment and enable consistent comparison across sensor-derived maps.

A normalized difference vegetation index (NDVI) threshold of 0.25 is applied to EnMap and Sentinel-2 to mask vegetated pixels. Because the WV3-SWIR data lack the VNIR spectral bands typically used to compute the NDVI (since the vegetation in the

study area is sparse), the vegetated pixels are manually extracted based on the historical imagery of Google Earth Pro, minimizing misclassification for the WV3-SWIR data. The Sentinel-2 NDVI mask is resampled to WV3-SWIR (3.7 m and 30 m) to cross-check the manual procedure. Potential subjectivity associated with manual vegetation masking is addressed through comparison with the Sentinel-2 mask resampled to WV3-SWIR spatial resolutions, indicating consistent results between methods.

Subsequently, all five datasets are processed using SAM and LSU, integrating endmembers from USGS and JPL spectral libraries. In the framework of SAM, the spectral vectors of five USGS endmembers (diaspore, hematite, goethite, kaolinite, and calcite) and five JPL endmembers (anatase, hematite, goethite, kaolinite, and calcite) are used. The threshold angle for SAM is set to 0.25 radians for EnMap (30 m), Sentinel-2 (10 m and 30 m), and WV3-SWIR (3.7 m and 30 m). Despite different signal-to-noise ratios (SNRs) and spectral resolutions across the satellite data, a fixed threshold is defined to point out similarities and differences between these satellite data outputs, enabling direct cross-comparison.

With the unconstrained LSU we create the abundance images for each mineral and a residual error image, which highlights pixels with the highest unmixing errors and is used to exclude unreliable pixels [26,53]. After unmixing, all negative values are set to 0, followed by pixel abundance normalization, so that the fractions sum to one [15]. Unconstrained LSU is selected to create the abundance maps because (1) it reflects the real situation and/or cases when non-linear mixtures occur and/or there is a spectral variability of the spectral signature of an endmember within the image or more endmembers exist within the pixel than those used as input in the model, (2) it produces negative values that are an indicator of the suitability of the endmembers used and/or the presence of other materials within the pixel that have not be taken into consideration, (3) the imposed constraints force the model to calculate positive abundances of the specific endmembers used as input in the model.

For the interpretation of results, we group the values of each method. In the case of SAM, the angle values range from low (0) to high (0.25). We break down the range of the angle values as follows: 0–0.10 is considered low, 0.10–0.15 as moderate, 0.15–0.20 as high, and values 0.20–0.25 as very high. The LSU abundance values range from low (0) to high (1). We also categorize the range of abundance values as follows: 0–0.20 is considered low, 0.20–0.50 as moderate, 0.50–0.70 as high, and values 0.70–1.00 as very high. To enhance clarity, we note that for SAM, low-angle values suggest a higher possibility of the mineral being present, while high-angle values increase the probability of a mineral being absent. An LSU low abundance value indicates a low presence of a mineral, whereas a high abundance value indicates a strong presence of the mineral in the study area.

It is crucial to mention that the field results recognize boehmite as a key component in at least some samples; however, the boehmite spectral signature is not detected either in the USGS or JPL library. This is because (1) boehmite is chemically indistinguishable from diaspore and (2) if its spectral signature were available, considering specifically the Al-OH main absorption feature of diaspore and boehmite, its position (within 2.20–2.30 nm) is most probably not very different between the two spectra. The boehmite absorption is probably shifted to slightly longer wavelengths than the corresponding diaspore one (by ~4–6 nm) but probably cannot be detected by the satellite sensors used in this study, due to each sensor's bandwidths, namely 10 nm for EnMap-SWIR bands, 55–88 nm for World View 3-SWIR bands, and two SWIR bands for Sentinel-2. Therefore, we shall hereafter use the spectral signature of diaspore interchangeably for boehmite. From this point onward, the term AlOOH will be used to refer to both diaspore and boehmite. Validation of AlOOH is thus performed using the diaspore spectral signature and the boehmite as detected by the laboratory analyses.

2.6. Ground Truth and Accuracy Assessment

Common error matrices are based on "one-class" per-pixel classifications. Accuracy assessment is challenging in sub-pixel mapping since many mineral classes could be traced in a single pixel [54], something which is relevant to this study: two or more classes (minerals) are distinguished for each sampling point, making the use of common error matrices challenging.

For each ground control point (GCP), we detect more than one mineral with the XRD analysis, indicating more than one label (mineral) per instance. Consequently, satellite-derived spectral values corresponding to each GCP are extracted for validation against the in situ XRD results. Similarly, satellite-based mineral mapping also identify multiple minerals within the same pixel corresponding to each GCP. In more detail, for each GCP's pixel and each mineral, a binary value is assigned (1 if the mineral is detected by the satellite sensor at the same pixel/GCP and 0 otherwise). Accordingly, a binary confusion matrix is then computed for each mineral to quantify the numbers of true positives (TPs), true negatives (TNs), false positives (FPs), and false negatives (FNs), from which the statistical metrics are calculated.

The model's predictions are assessed using the following standard metrics: true positive (TP) indicates the model correctly predicted the presence of the mineral (agreement between prediction and actual existence), true negative (TN) indicates the model correctly predicted the absence of the mineral (agreement between prediction and actual non-existence), false positive (FP) indicates the model incorrectly predicted the presence of a mineral that is not actually present, and false negative (FN) indicates the model failed to detect a mineral that is actually present. When TP and FP (or FN) are not available, the precision or recall cannot be computed (mineral is not mapped or validation points do not intersect the mapped pixels); therefore, the F1-score is also not computed.

Recall, precision, and F1-score are the parameters with which we calculate statistical metrics. Recall is the proportion of correctly predicted positive samples among all samples in the actual class (TP/TP + FN), precision is the percentage of actual positive observations out of the observations that are predicted to be positive (TP/TP + FP), and F1-Score is the balance between precision and recall (2TP/2TP + FP + FN) [55–57]. The accuracy of each class is given with the F1-score [57].

3. Results

3.1. Endmember Spectra

The spectral signatures of the USGS endmembers (Table 3 and Figure 2) show absorption features at the following wavelengths: Diaspore characteristic absorption occurs at 1780/2014/2191 nm (EnMap) and 1730/2202 nm (WV3-SWIR) but not in Sentinel-2. Hematite has its characteristic absorption at 566/879 nm and low absorption (less than 0.10) in SWIR (EnMap), characteristic absorption at 559/864 nm (Sentinel-2), and low absorption (less than 0.10) in WV3-SWIR. Goethite has its characteristic absorption at 501/664 nm and low absorption (less than 0.15) in SWIR (EnMap), main absorption in 492/943 nm (Sentinel-2), and low absorption (less than 0.10) at 1730/2202 nm in WV3-SWIR. Kaolinite has its characteristic absorption at 2165/2207 nm and low absorption (less than 0.10) in VNIR (EnMap), low absorption (less than 0.10) at 703/832/943 nm in Sentinel-2, and a characteristic absorption at 2202 nm in WV3-SWIR. Finally, calcite shows characteristic absorption at 2337 nm and low absorptions (less than 0.10) at VNIR and SWIR spectral bands (EnMap), low absorptions at 943 nm of Sentinel-2, and characteristic absorption at 2164 nm in WV3-SWIR.

Table 3. Main absorption of minerals: USGS endmembers.

Mineral	EnMap Absorption (nm)	Sentinel-2 Absorption (nm)	WV3-SWIR Absorption (nm)
Diaspore	1780/2014/2121	-	1730/2202
Hematite	566/879	559/864	Low absorption
Goethite	501/664	492/943	Low absorption
Kaolinite	2165/2207	Low absorption	2202
Calcite	2337	Low absorption	2164

The spectral signatures of the JPL endmembers (Table 4 and Figure 2) show absorption at the following wavelengths: Hematite has its characteristic absorption at 535/871 nm and low absorption (less than 0.15) in SWIR (EnMap), characteristic absorption at 559/864 nm (Sentinel-2), and low absorption (less than 0.10) at 1571 nm in WV3-SWIR. Goethite has its characteristic absorption at 482/960 nm and low absorption (less than 0.15) in SWIR (EnMap), characteristic absorption at 559/864 nm (Sentinel-2), and an almost flat spectrum in WV3-SWIR. Anatase has many low absorptions (less than 0.05) in VNIR-SWIR, with the highest absorption at 1967 nm. For Sentinel-2A and WV3-SWIR, an almost flat spectrum is observed. Kaolinite has its characteristic absorption at 2199 nm, but many low absorptions (less than 0.10) are observed in VNIR-SWIR (EnMap). Minor absorption is observed at 943.2 nm (Sentinel-2A) and 2163 nm (WV3-SWIR). Calcite has its characteristic absorption at 2337 nm, but many low absorptions (less than 0.10) are observed in VNIR-SWIR (EnMap). Low absorption is observed at 779 nm (Sentinel-2A) and 2163 nm (WV3-SWIR).

Table 4. Main absorption of minerals: JPL endmembers.

Mineral	EnMap Absorption (nm)	Sentinel-2 Absorption (nm)	WV3-SWIR Absorption (nm)
Anatase	Low absorptions	-	-
Hematite	535/871	559/864	Low absorption
Goethite	482/960	492/943	-
Kaolinite	2199	Low absorptions	2163
Calcite	2337	Low absorptions	2163

3.2. Cross-Sensor Analysis Description

This sub-section shows both methods' outputs across three satellite sensors to examine their spatial and spectral resolution and endmember characteristics in mine waste mapping. We present the results for the USGS (Figures 4 and 5, and Tables 5 and 6) and JPL (Figures 6 and 7, and Tables 7 and 8) endmembers. To maintain consistency hereon, the range of spectral angle values is named "angles", indicating the SAM results, and the abundance values are named "abundances", indicating the LSU results.

To achieve a comparison among the results, (1) we give the detection capability of each sensor for each method separately for the USGS and JPL endmembers and (2) we visually compare the results (rule or abundance images). With the visual interpretation, we present similarities and differences in the rule or abundance images, pointing out the mineral presence/absence in each image.

The interpretation of the results (USGS and JPL endmembers) is broken down into two aspects: (1) endmember spatial distribution assessment and (2) endmember angle and abundance evaluation as retrieved from rule or abundance images (visual interpretation).

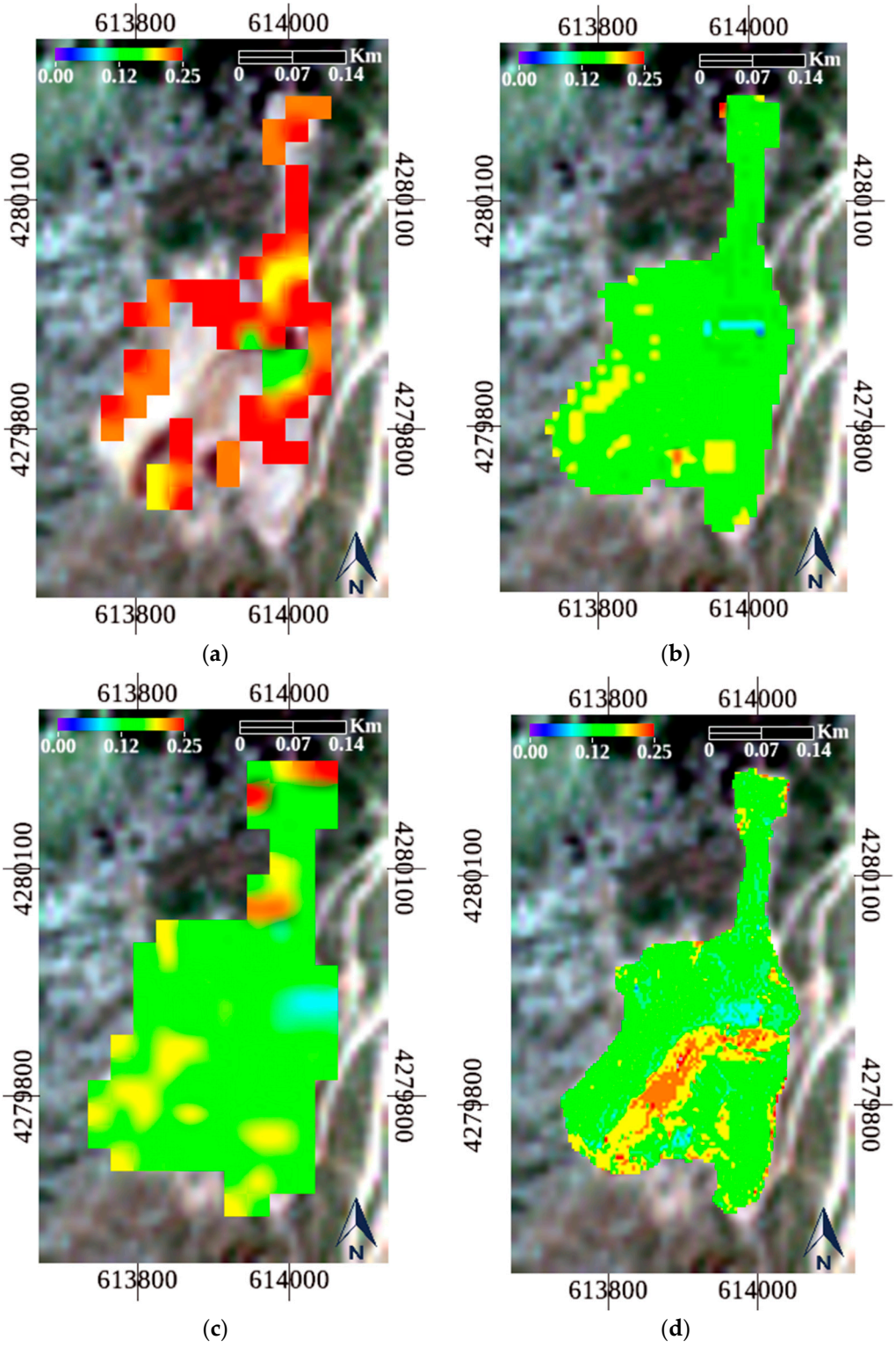


Figure 4. *Cont.*

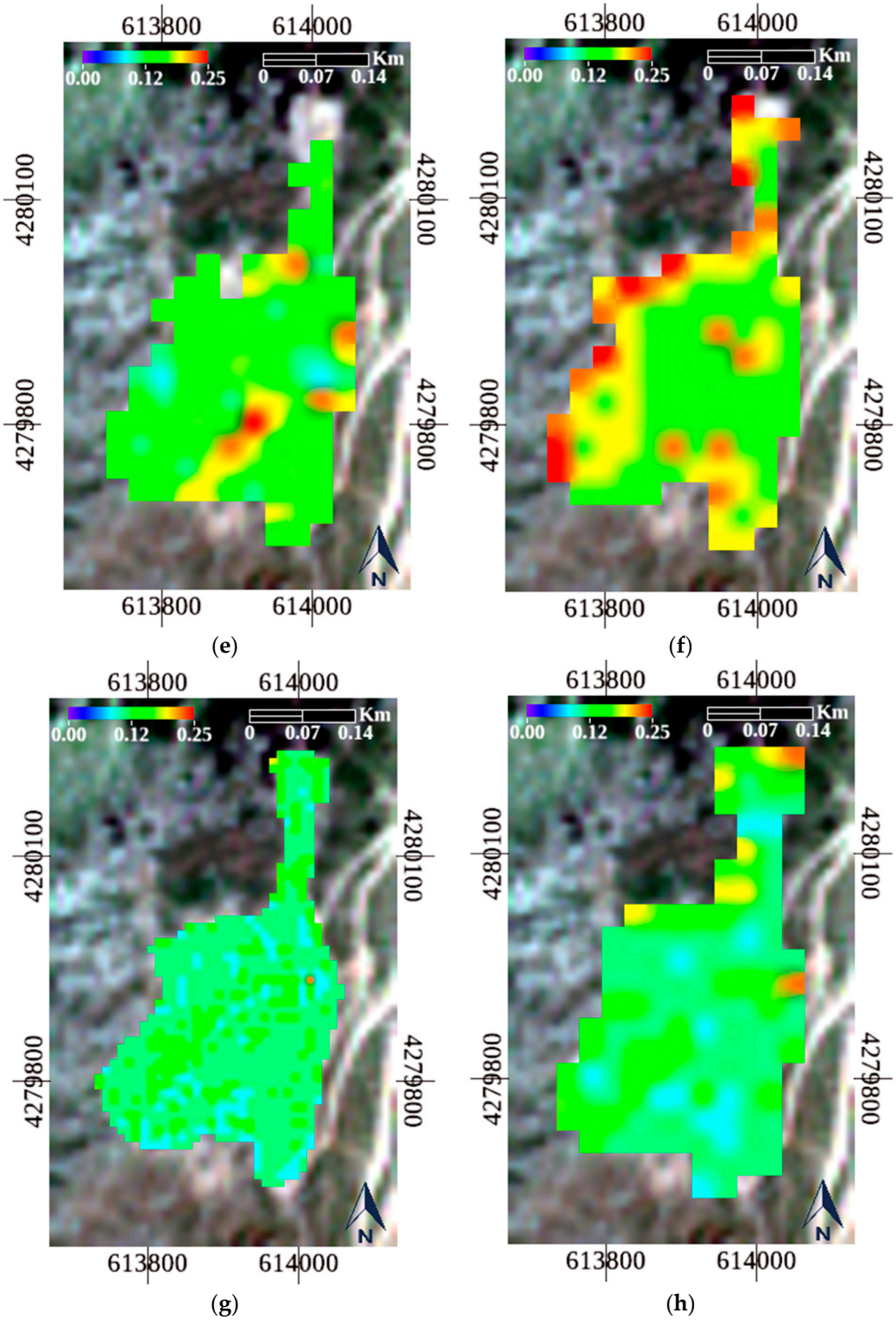


Figure 4. *Cont.*

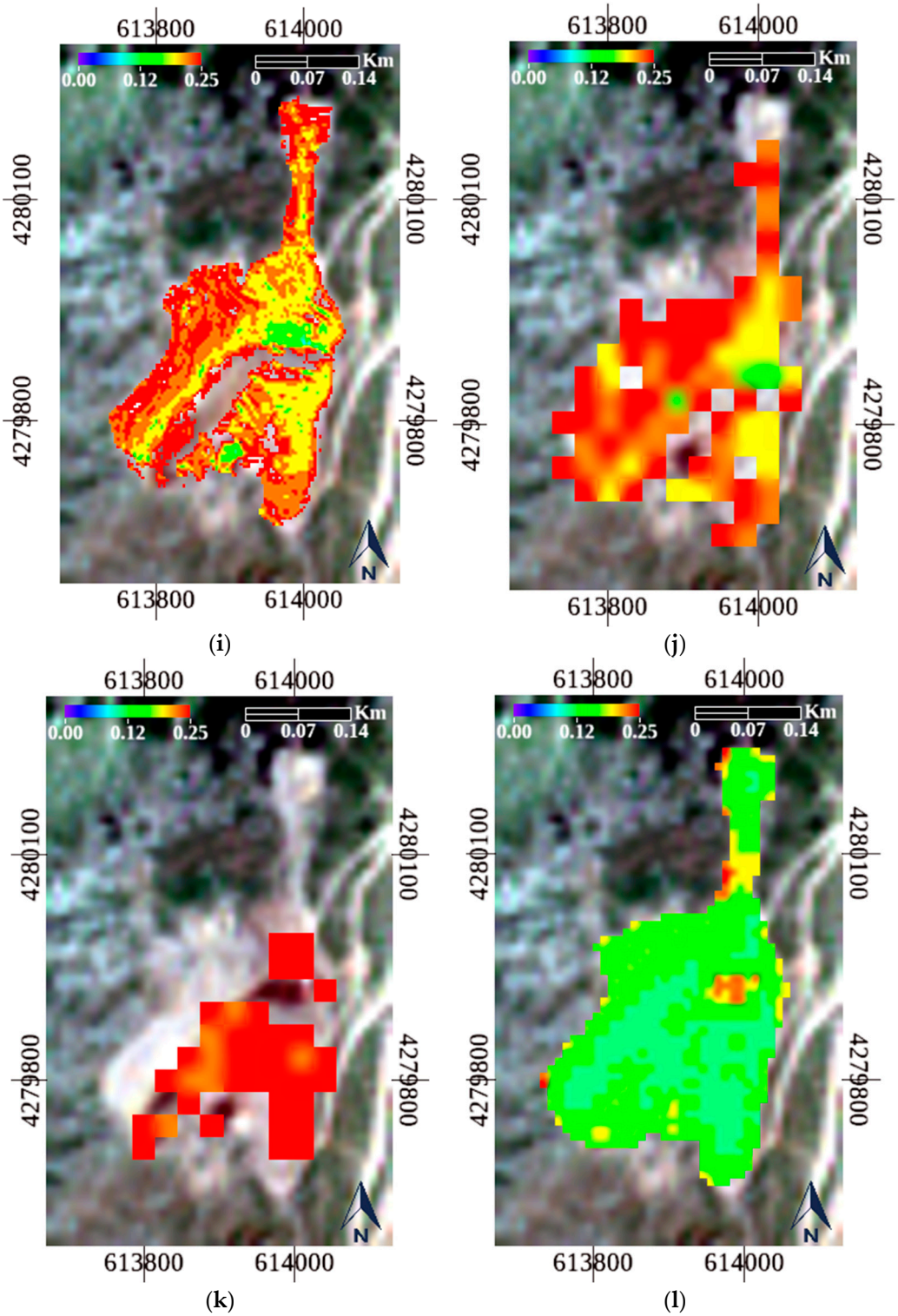


Figure 4. *Cont.*

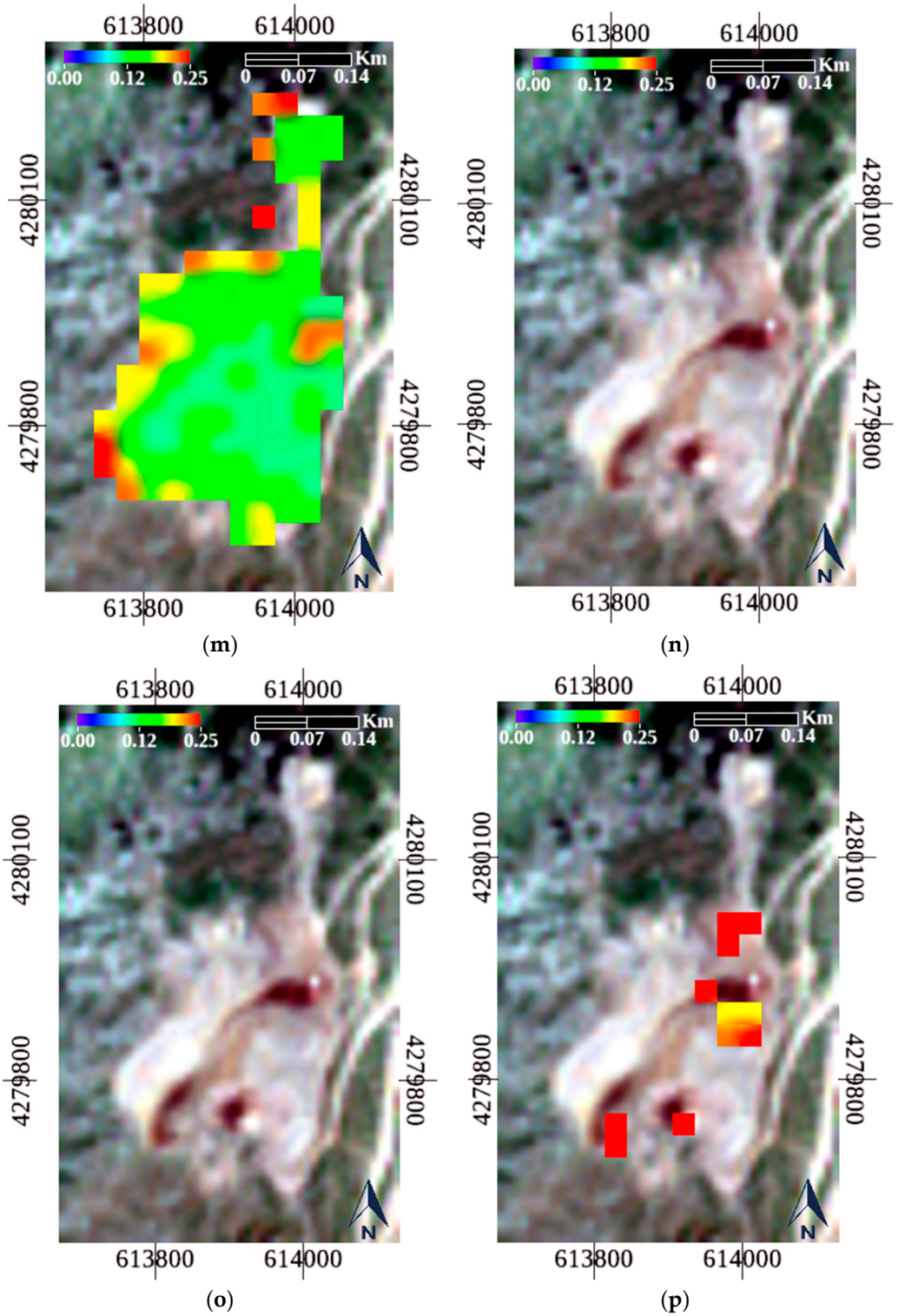


Figure 4. *Cont.*

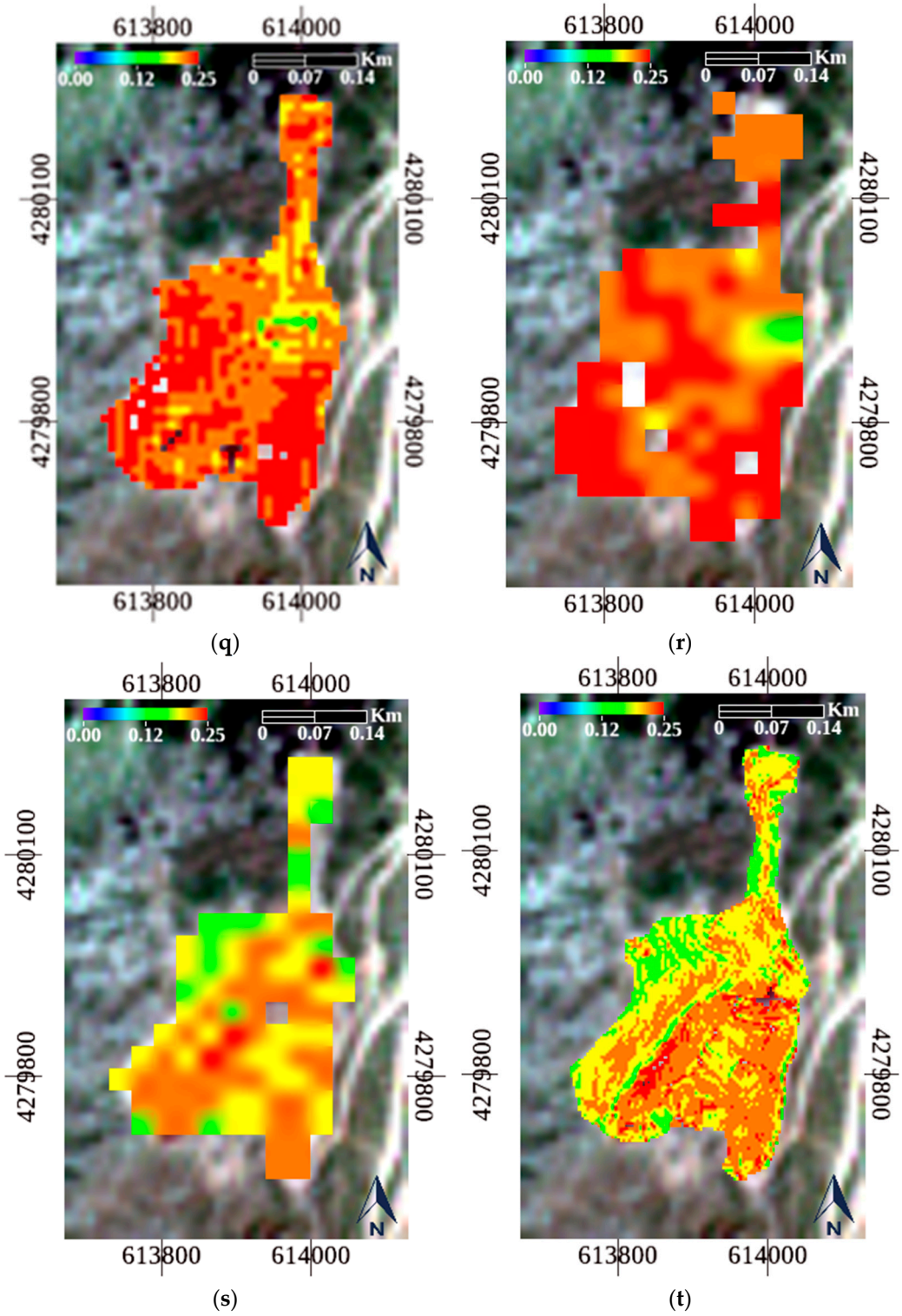


Figure 4. *Cont.*

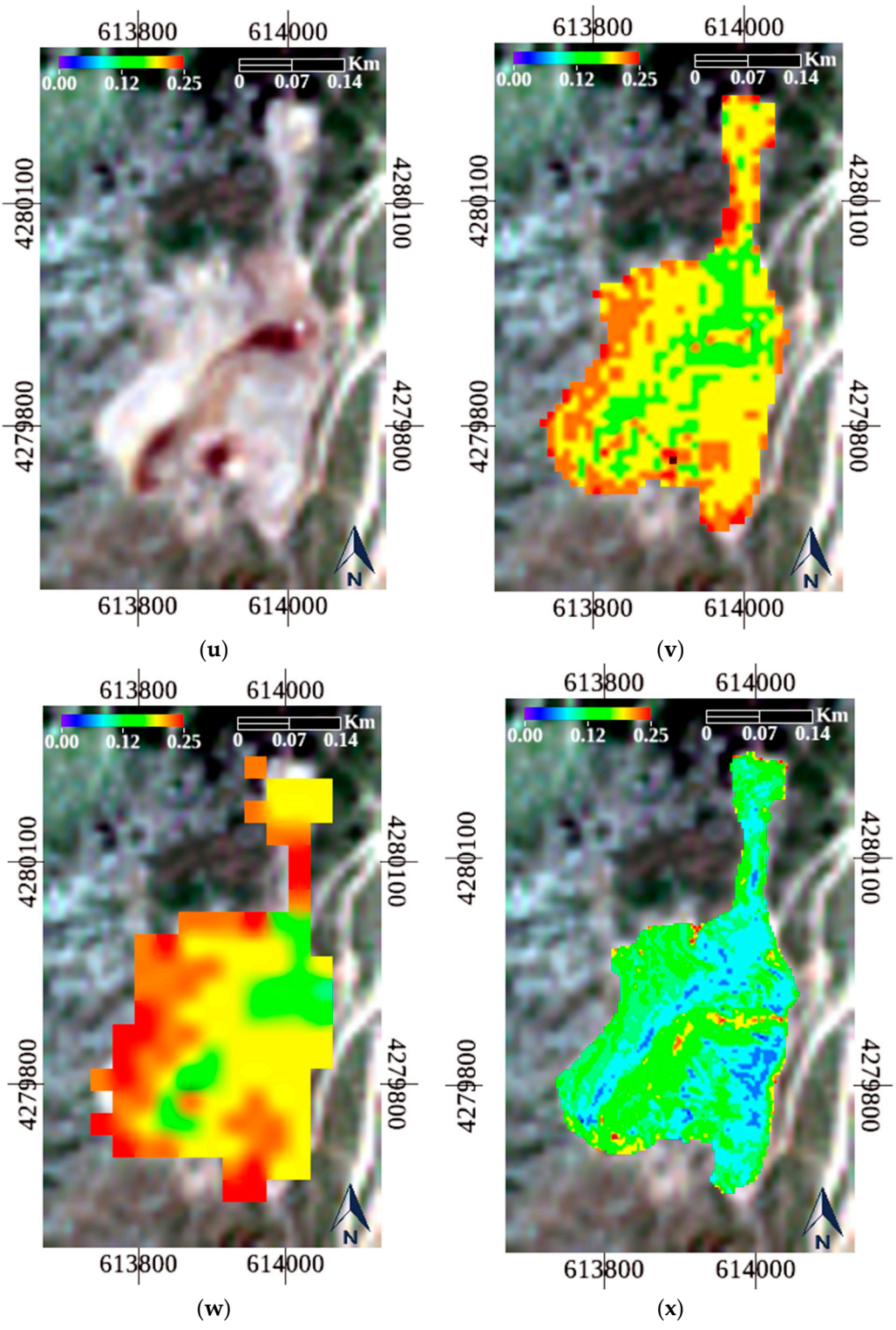


Figure 4. *Cont.*

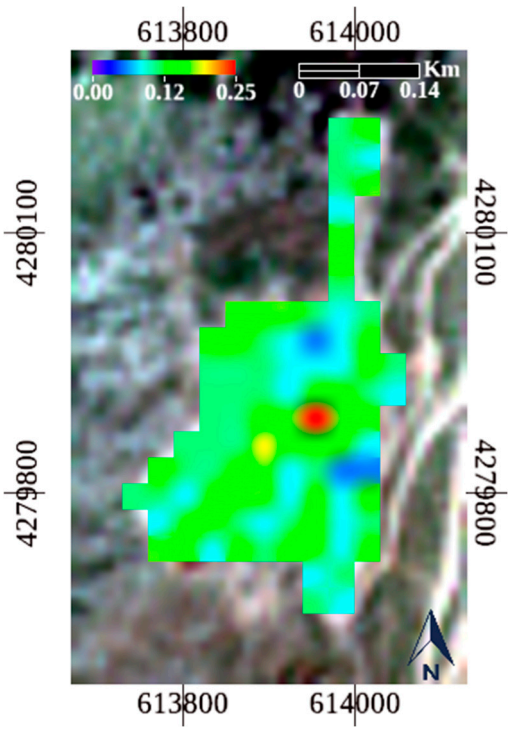


Figure 4. Classification maps (from top to bottom) of AlOOH (**a**–**e**), hematite (**f**–**j**), goethite (**k**–**o**), kaolinite (**p**–**t**), and calcite (**u**–**y**). The maximum angle threshold of 0.25 radians is common for the EnMap, Sentinel-2, and WV3-SWIR sensors. The first column corresponds to EnMap (30 m), the second and third columns to Sentinel-2 (10 m and 30 m), and the fourth and fifth columns to WV3-SWIR (3.7 m and 30 m). Endmembers are retrieved from the USGS spectral library. Classification colors range from low-angle threshold (blue) to high-angle threshold values (red). Basemap: the TCI of Sentinel-2 (26 June 2024).

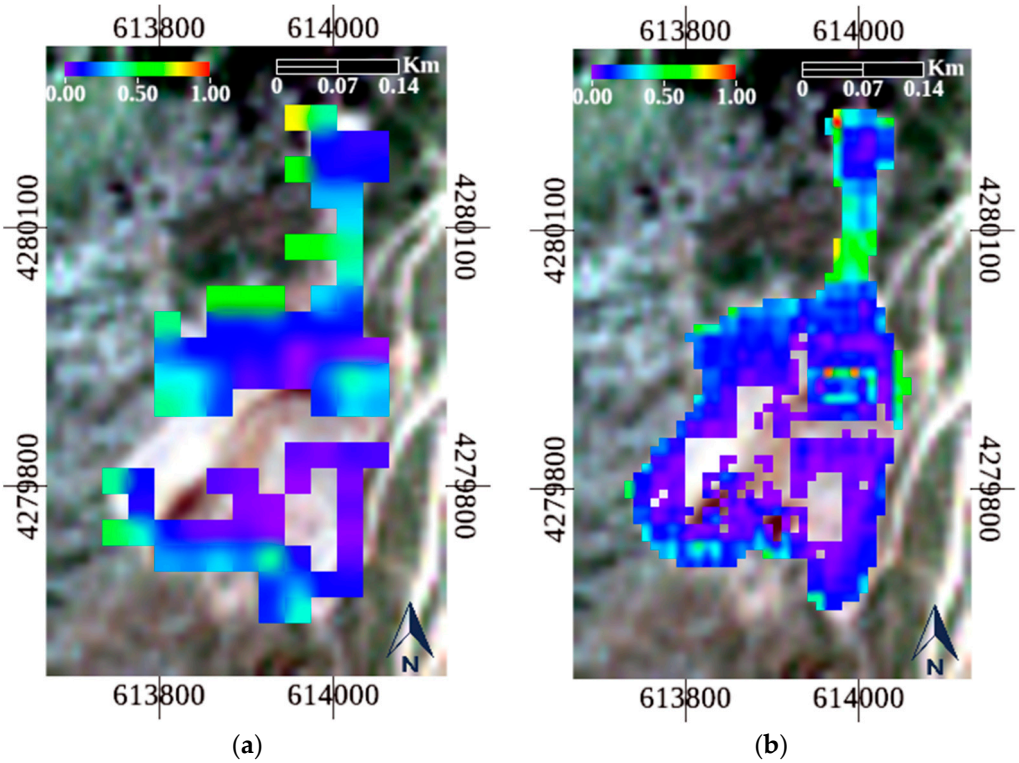


Figure 5. *Cont.*

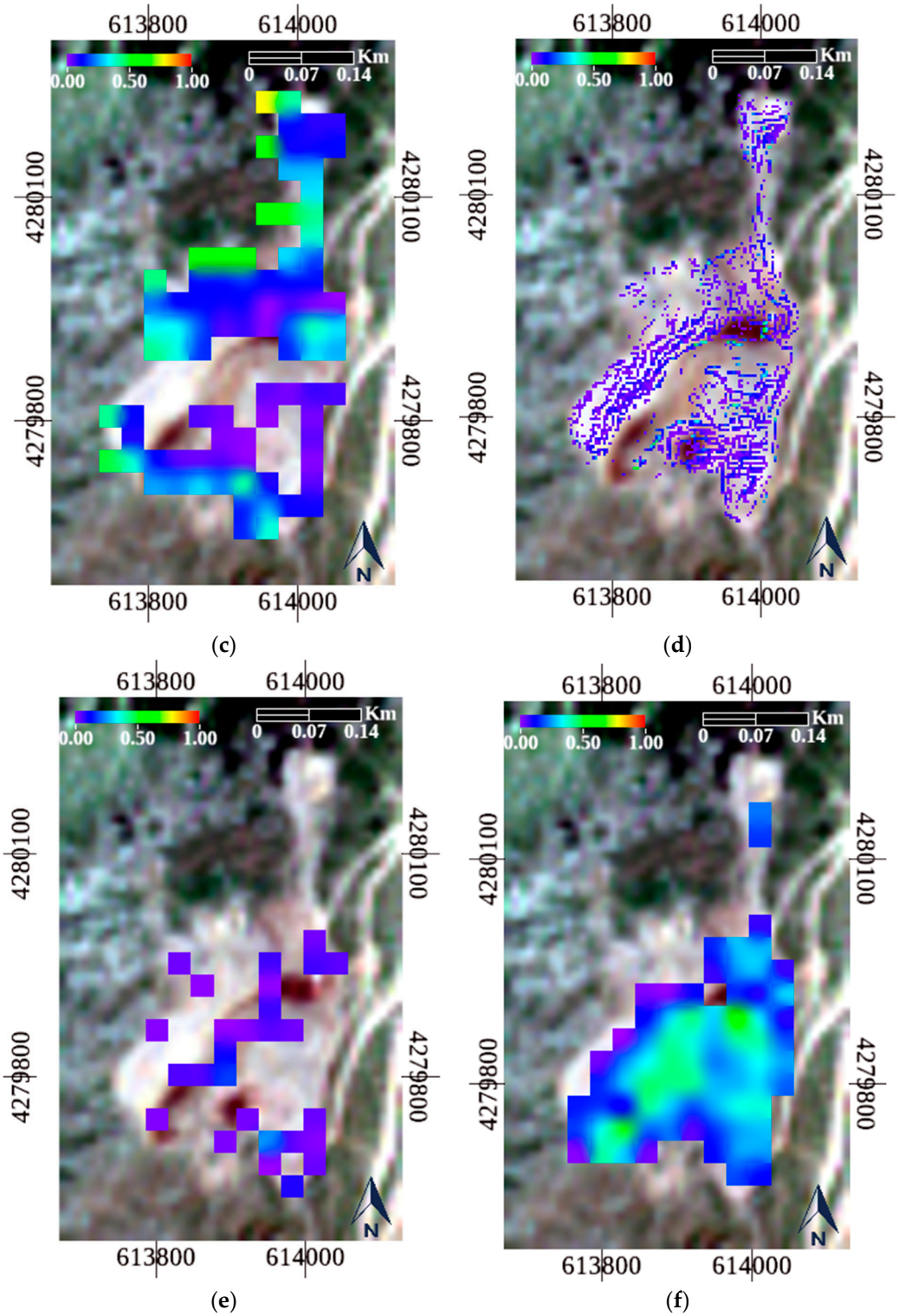


Figure 5. *Cont.*

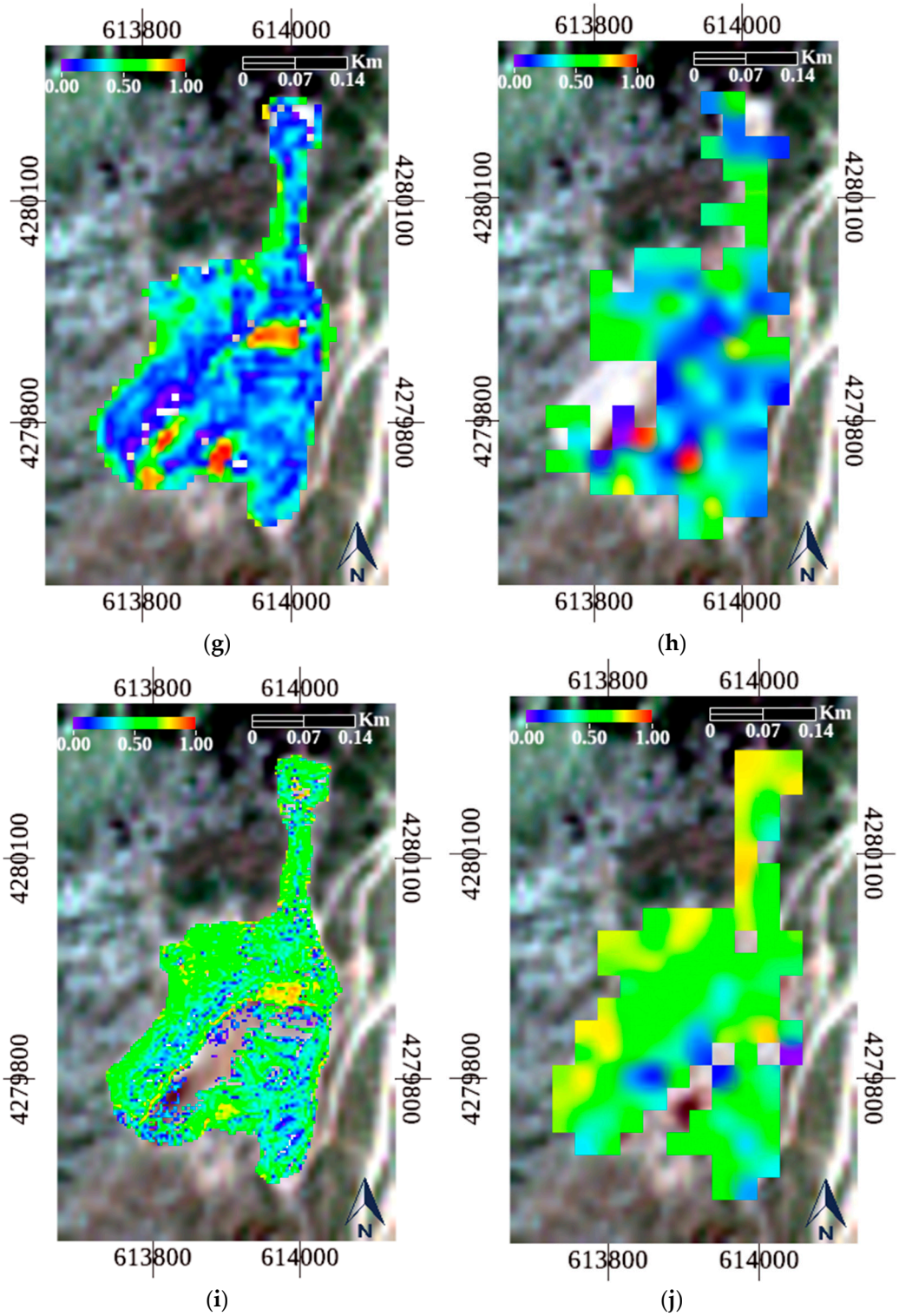


Figure 5. *Cont.*

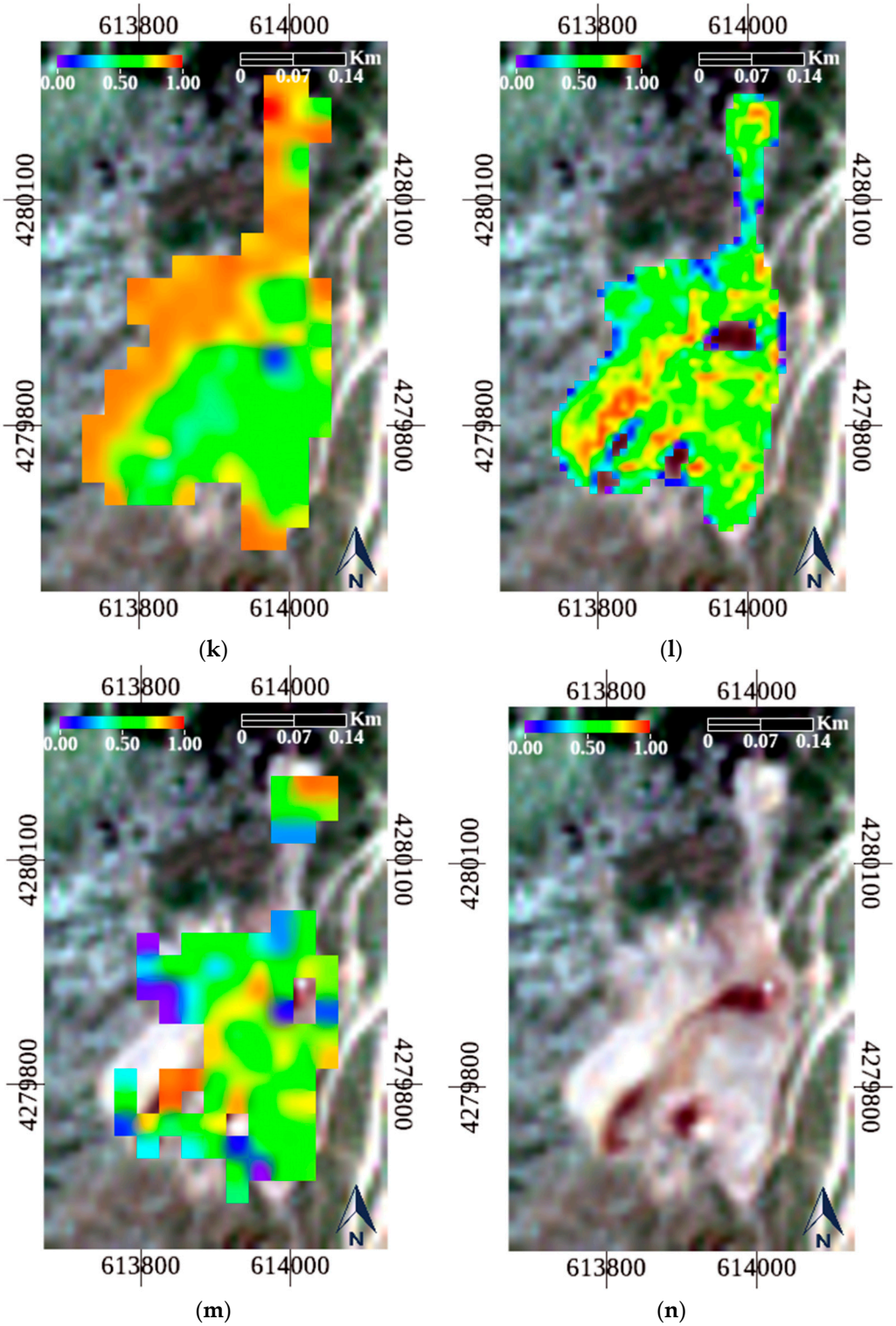


Figure 5. *Cont.*

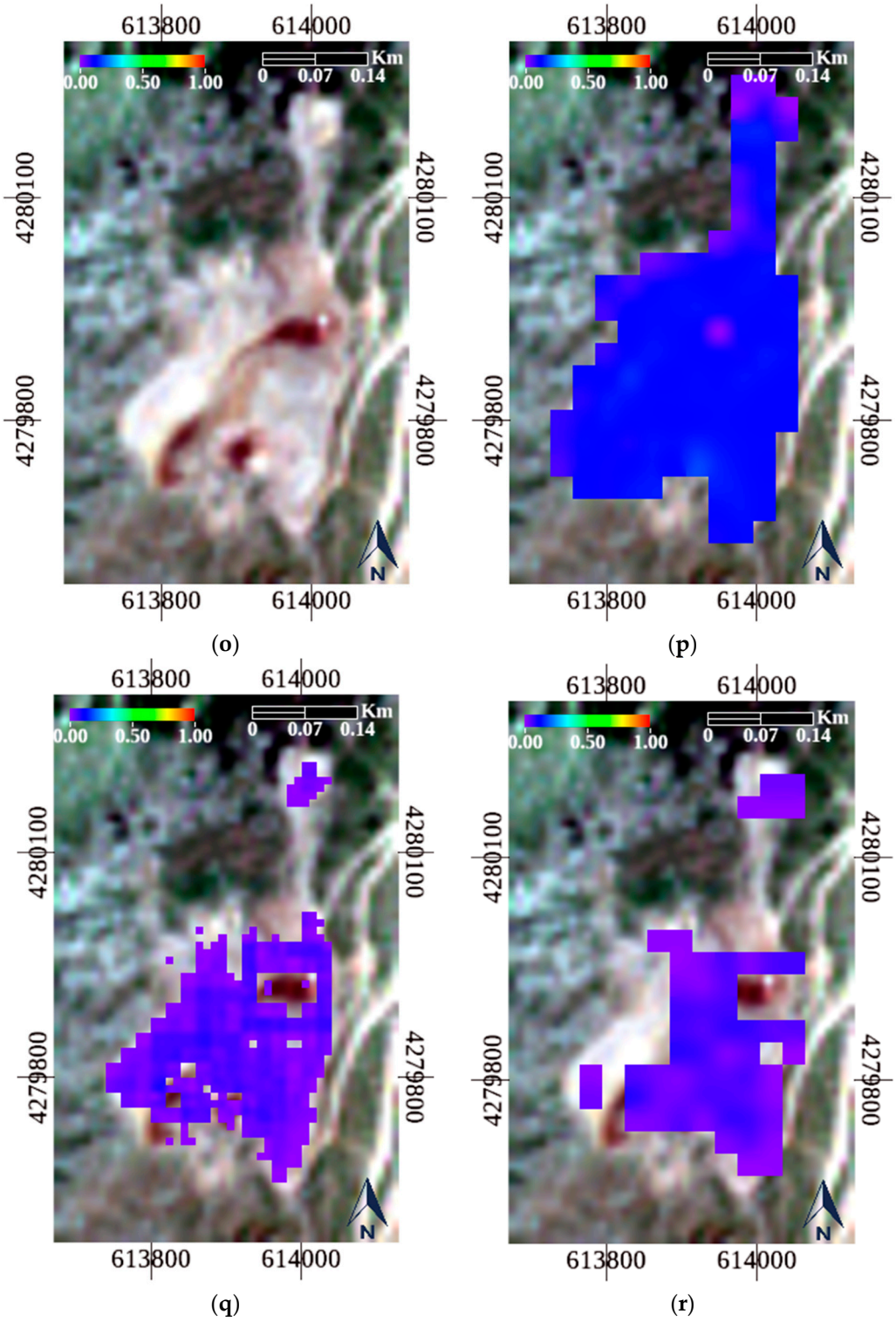


Figure 5. *Cont.*

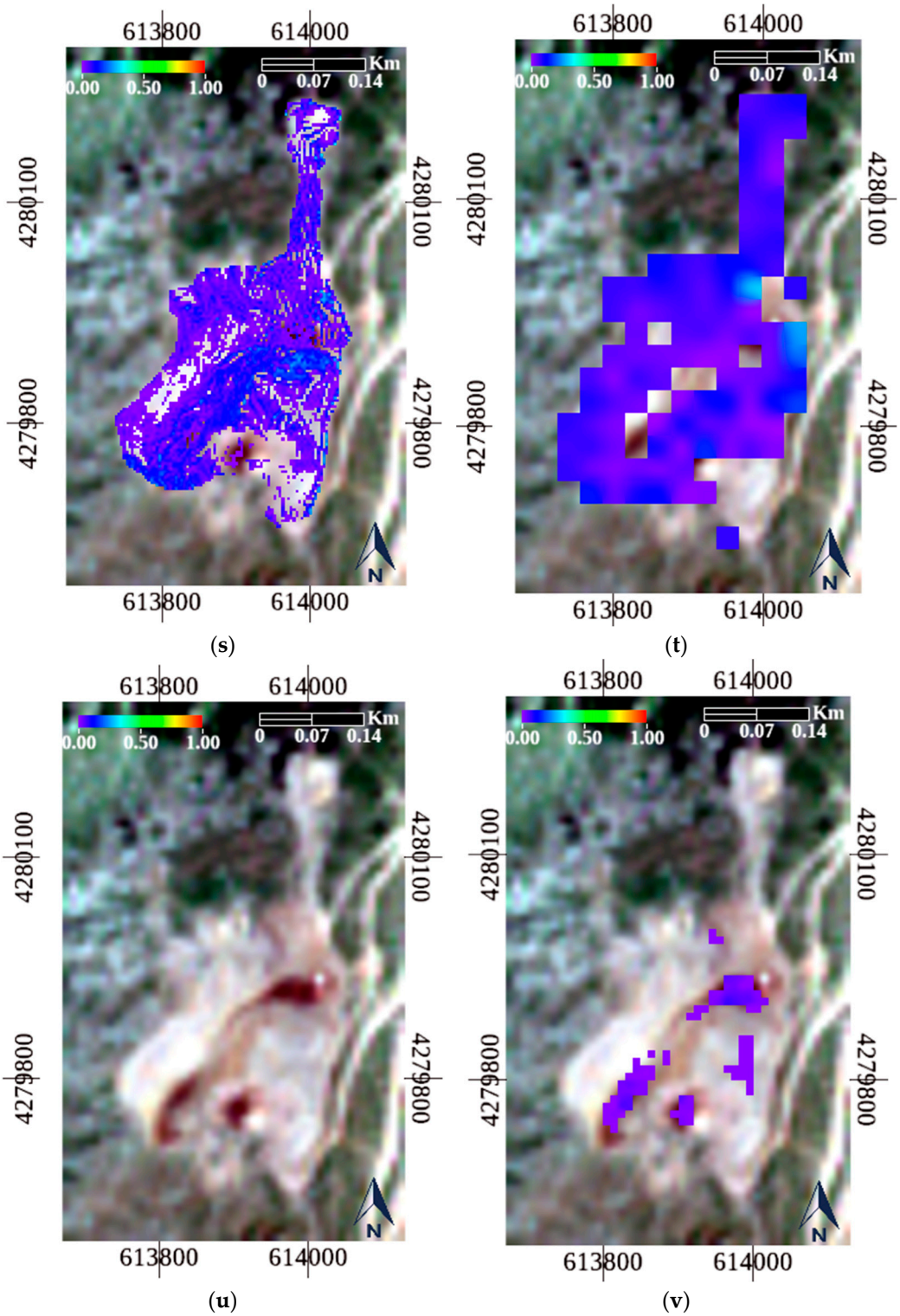


Figure 5. *Cont.*

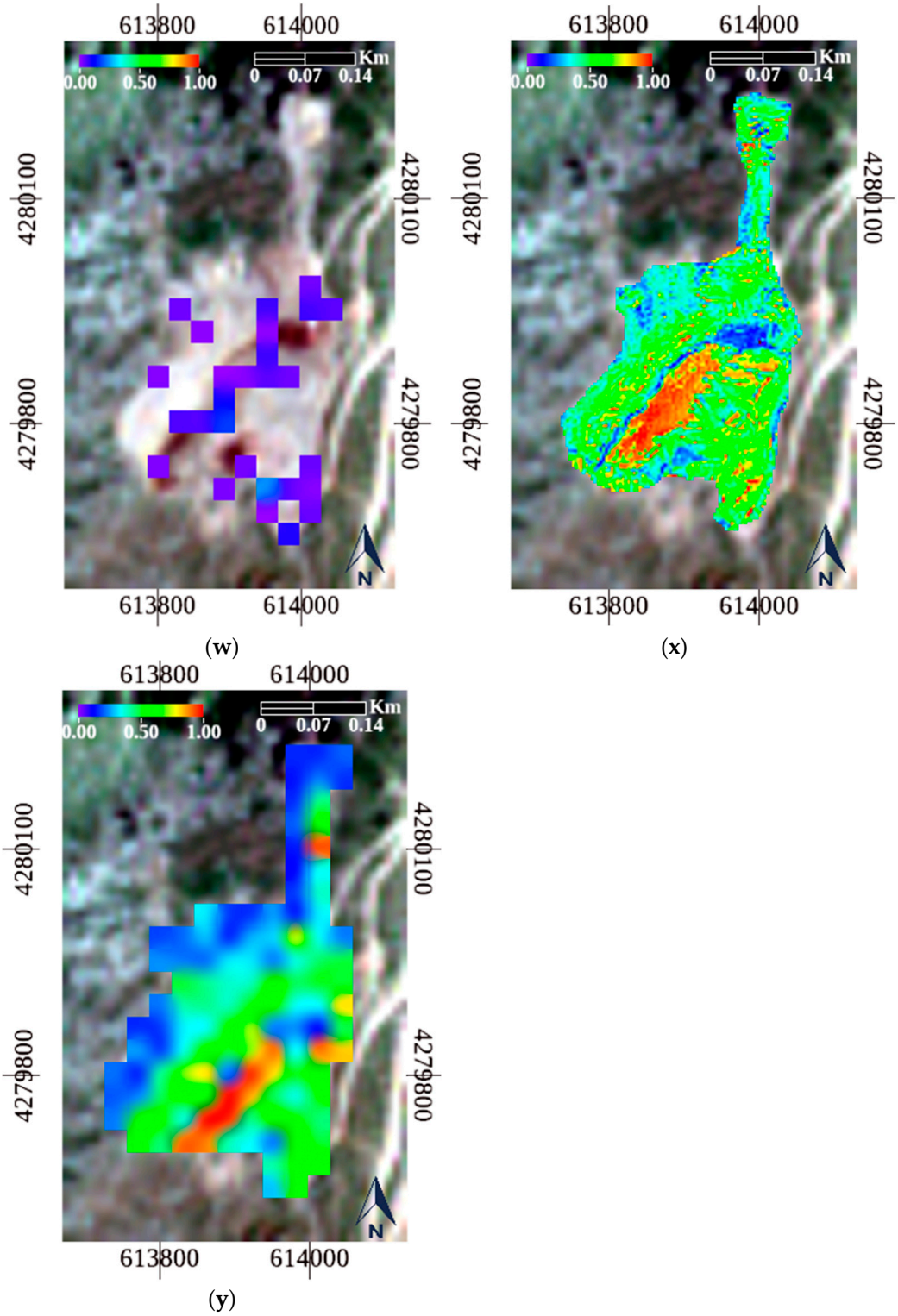


Figure 5. Abundance maps (from top to bottom) of AlOOH (**a**–**e**), hematite (**f**–**j**), goethite (**k**–**o**), kaolinite (**p**–**t**), and calcite (**u**–**y**). The first column corresponds to EnMap (30 m), the second and third columns to Sentinel-2 (10 m and 30 m), and the fourth and fifth columns to WV3-SWIR (3.7 m and 30 m). Endmembers are retrieved from the USGS spectral library. Abundance colors range from low, 0 (purple), to high, 1 (red), values. Basemap: the TCI of Sentinel-2 (26 June 2024).

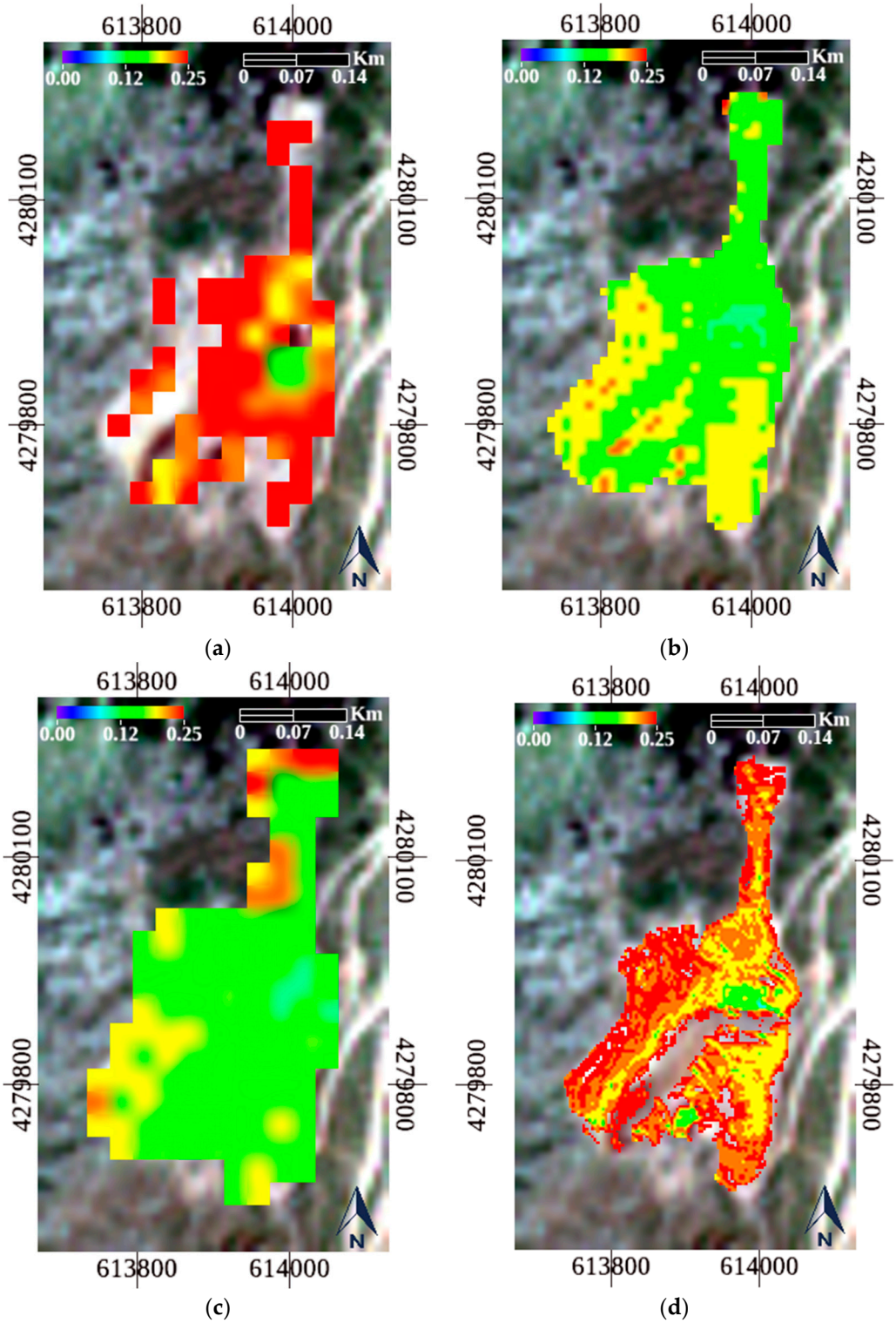


Figure 6. *Cont.*

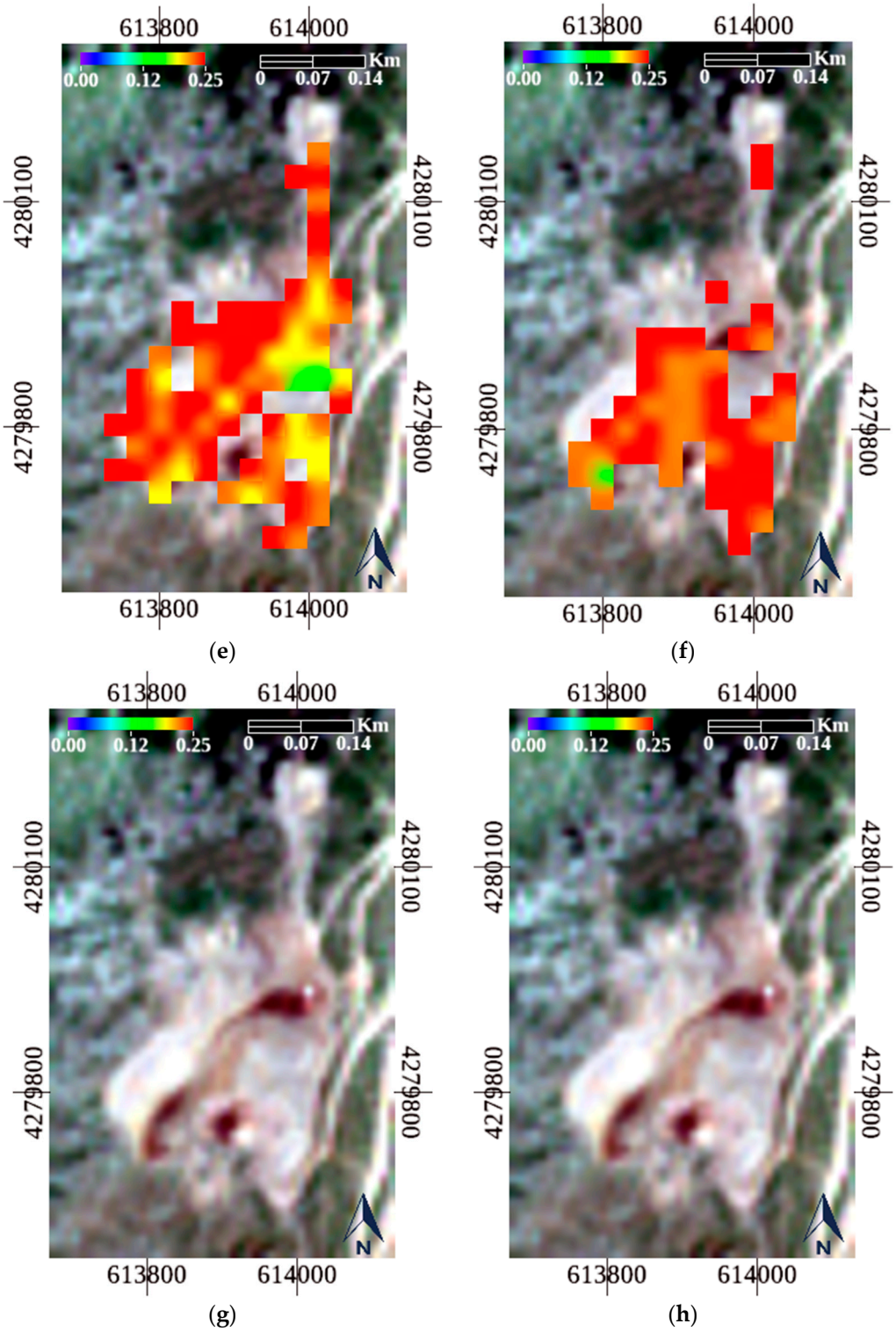


Figure 6. *Cont.*

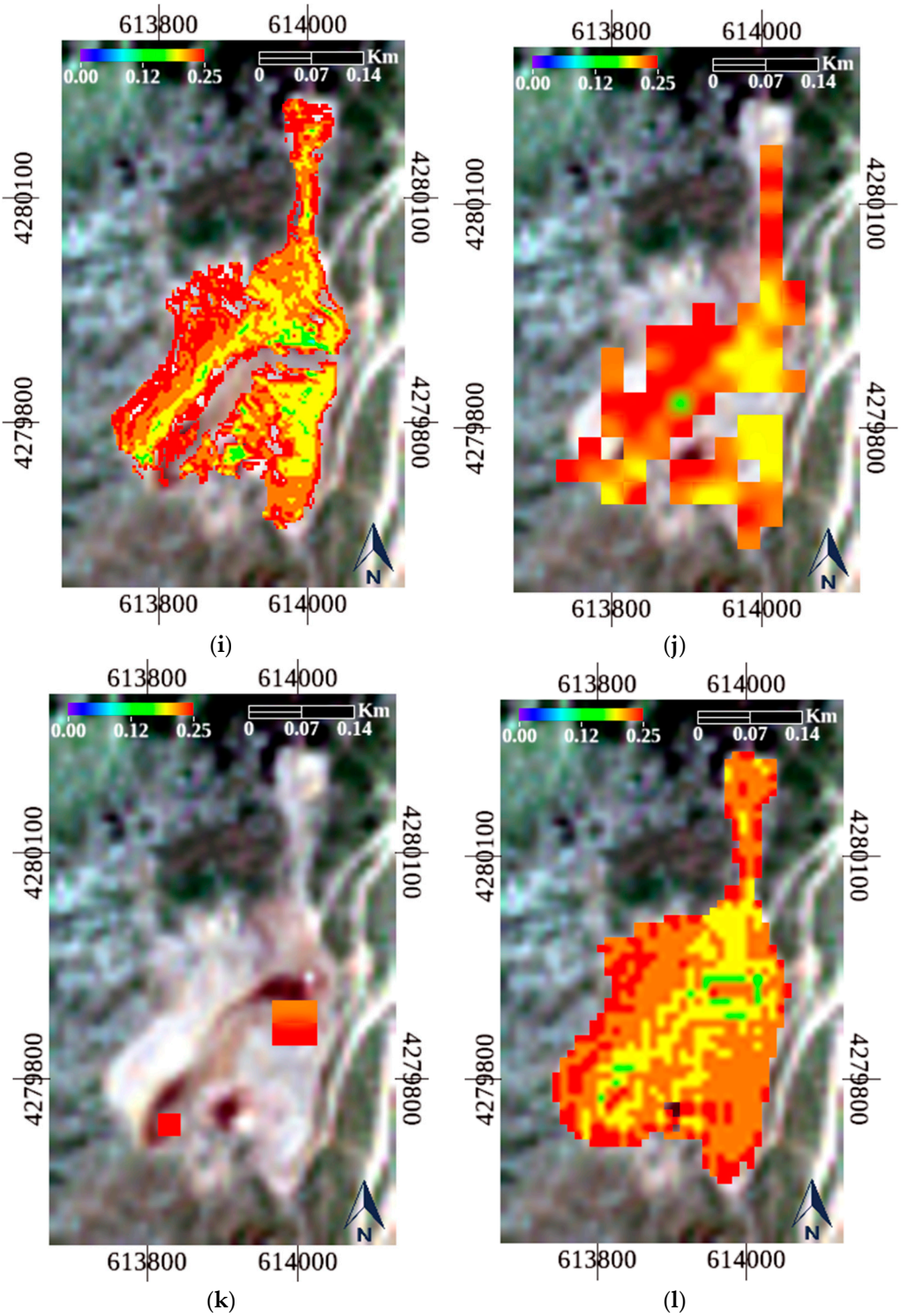


Figure 6. *Cont.*

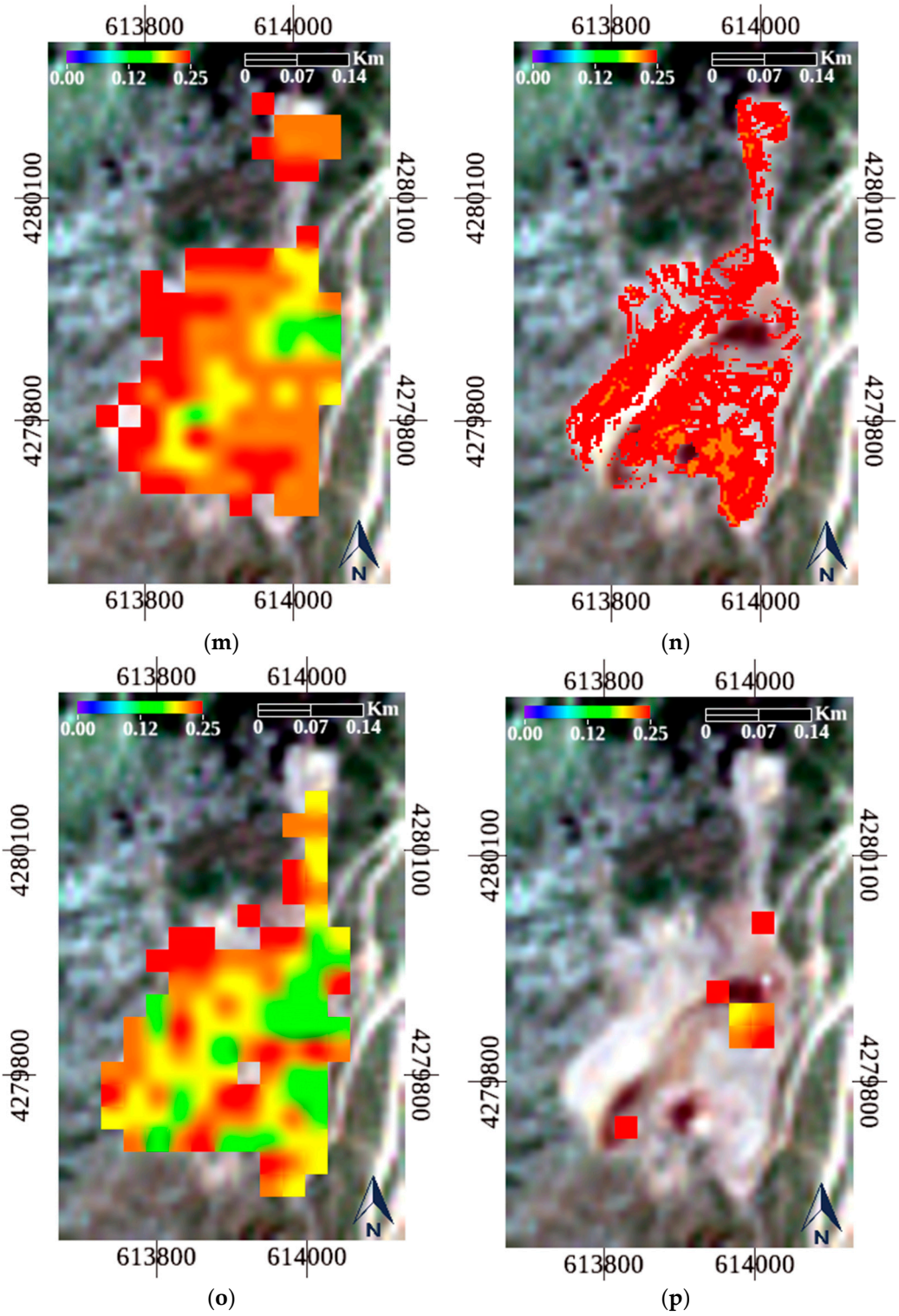


Figure 6. *Cont.*

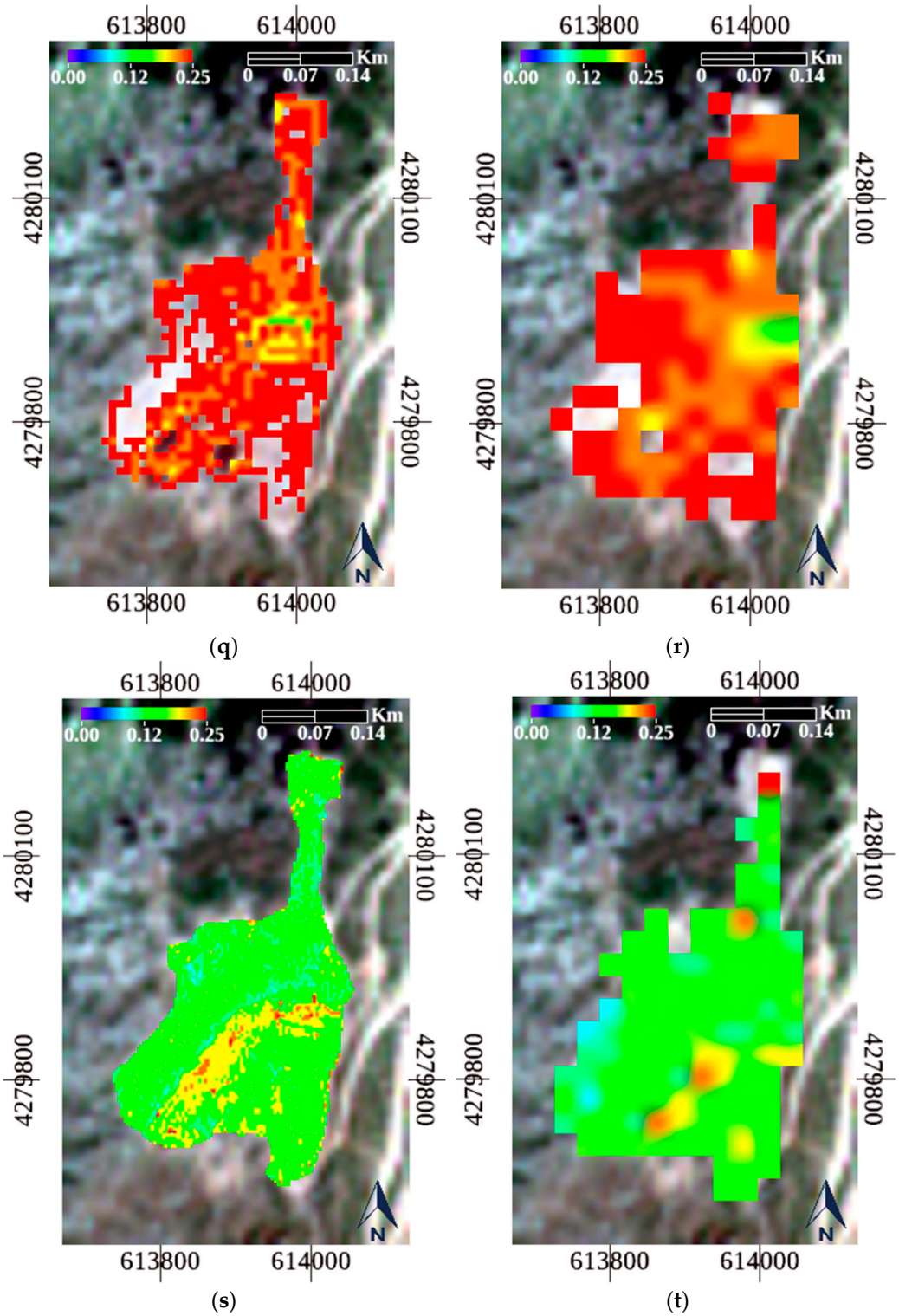


Figure 6. *Cont.*

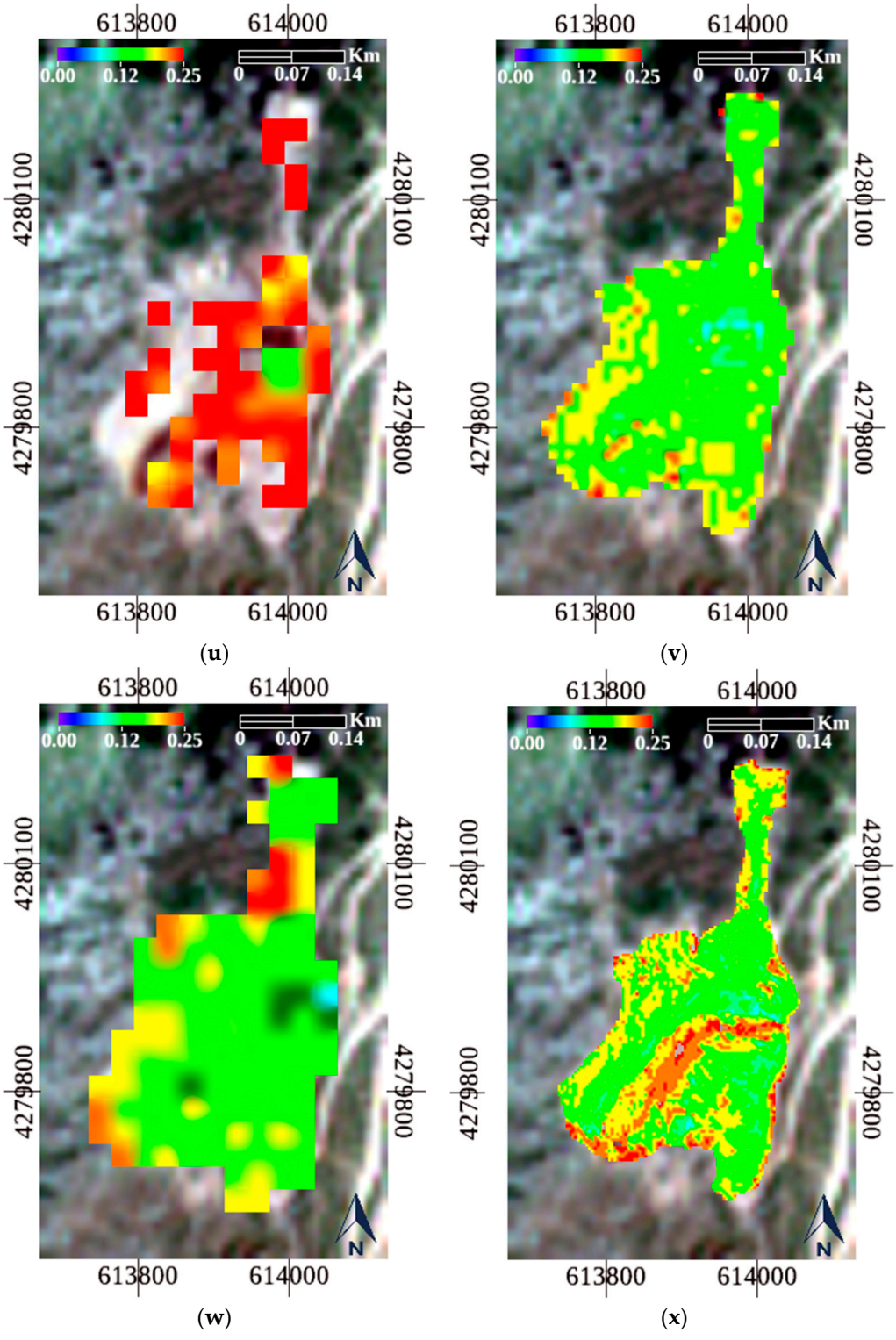


Figure 6. *Cont.*

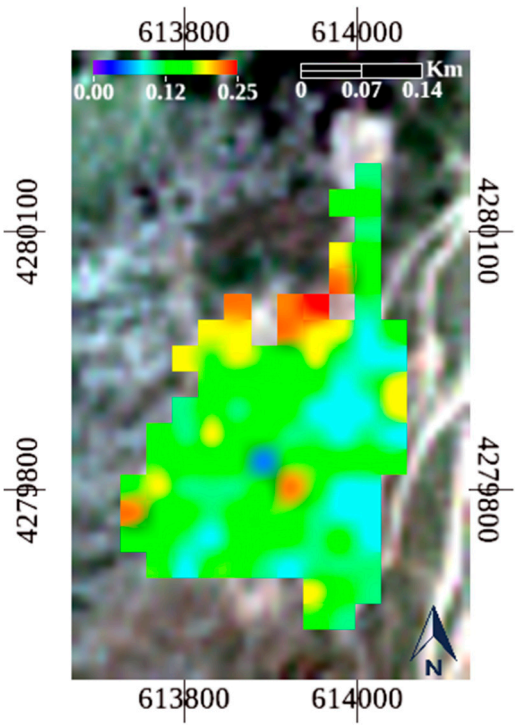


Figure 6. Classification maps (from top to bottom) of hematite (**a**–**e**), goethite (**f**–**j**), anatase (**k**–**o**), kaolinite (**p**–**t**), and calcite (**u**–**y**). The threshold angle is 0.25 radians, common for EnMap, Sentinel-2, and WV3-SWIR. The first column corresponds to EnMap (30 m), the second and third columns to Sentinel-2 (10 m and 30 m), and the fourth and fifth columns to WV3-SWIR (3.7 m and 30 m). Endmembers are retrieved from the JPL spectral library. Classification colors range from low-angle threshold (blue) to high-angle threshold values (red). Basemap: the TCI of Sentinel-2 (26 June 2024).

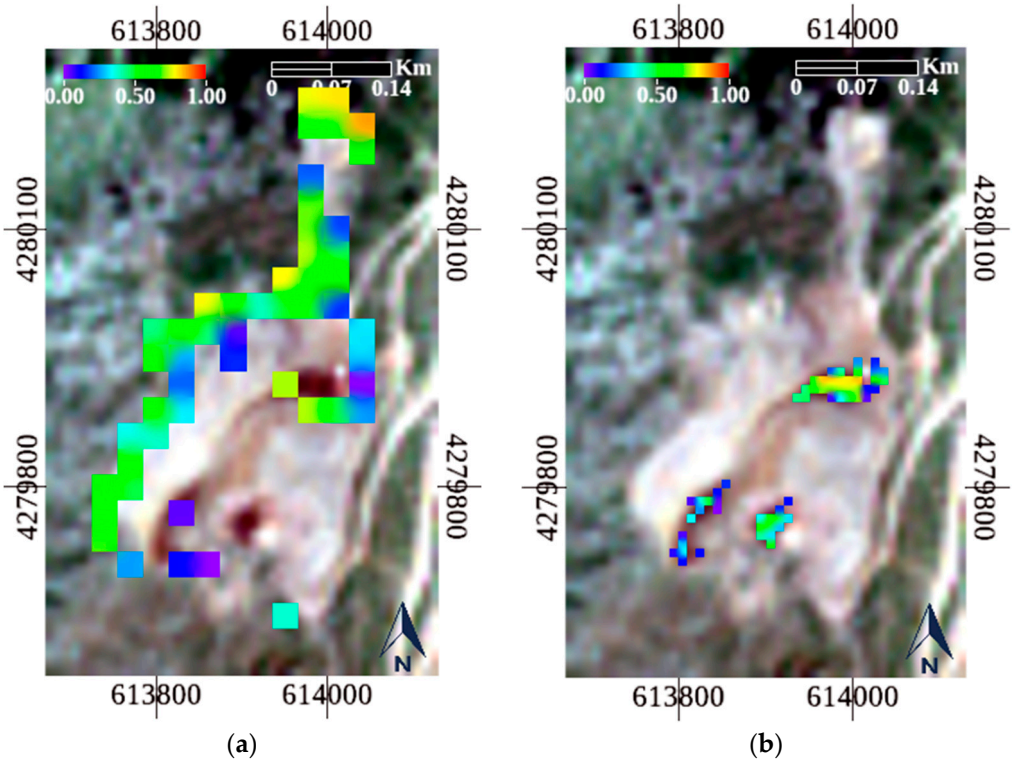


Figure 7. *Cont.*

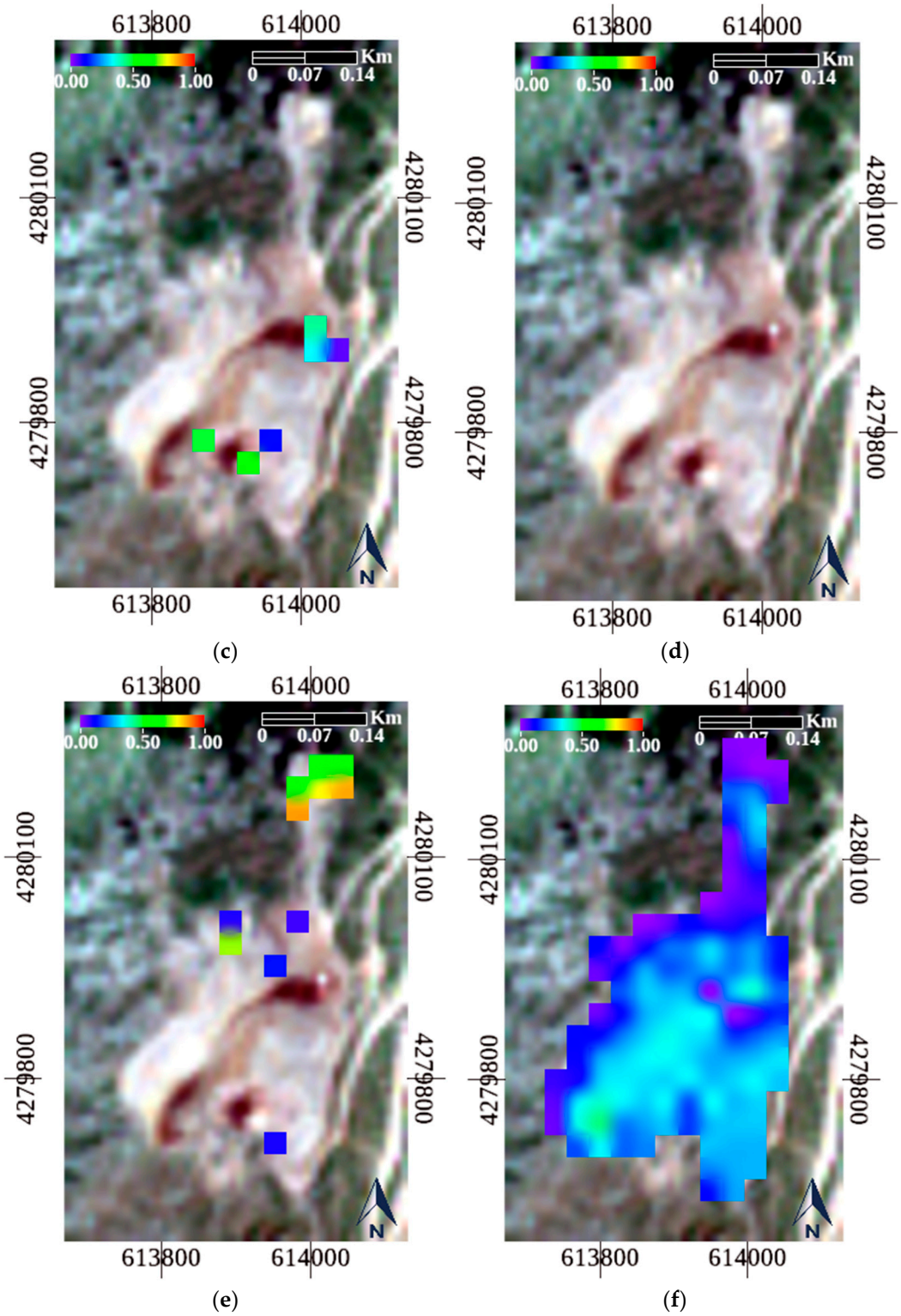


Figure 7. *Cont.*

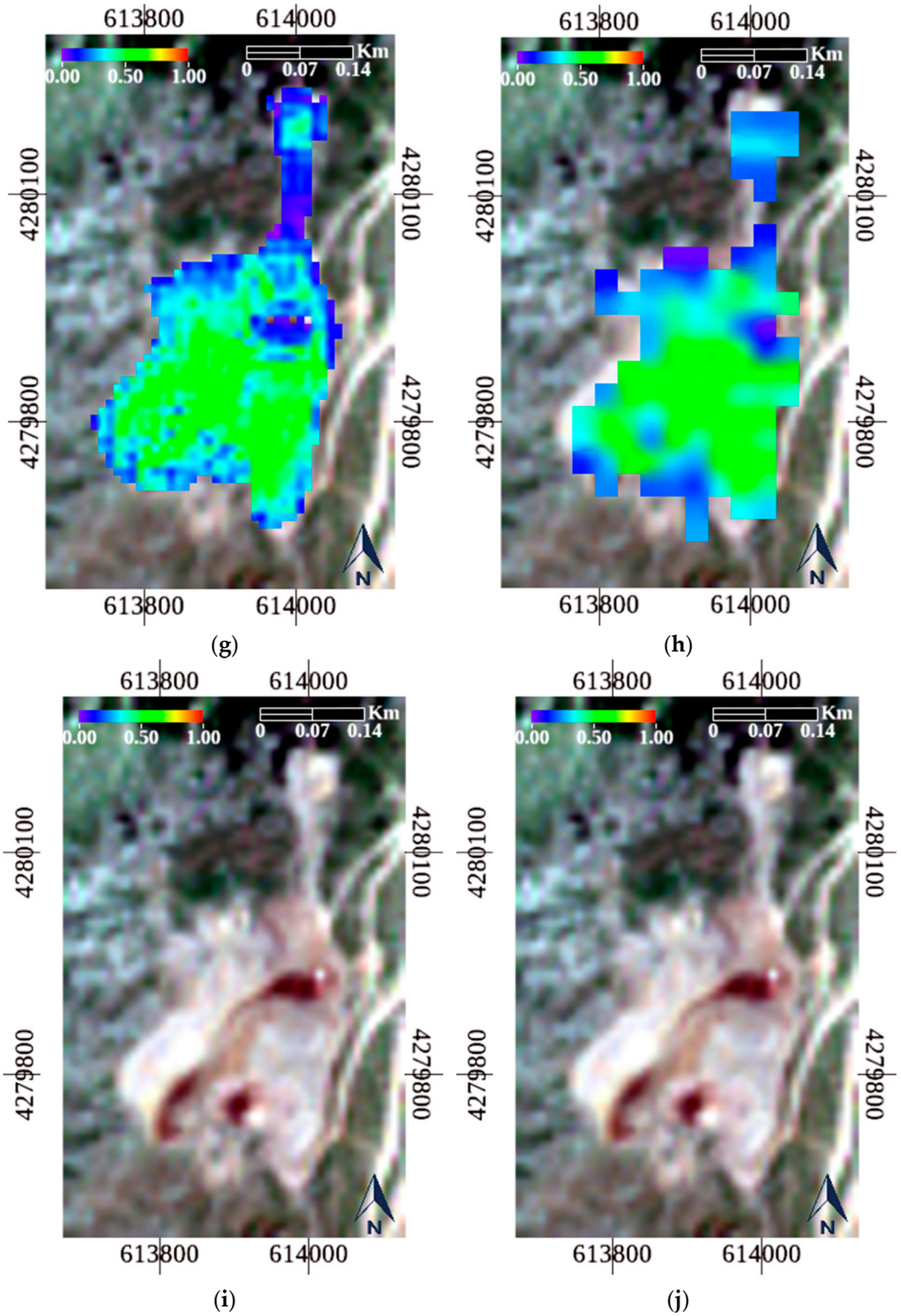


Figure 7. *Cont.*

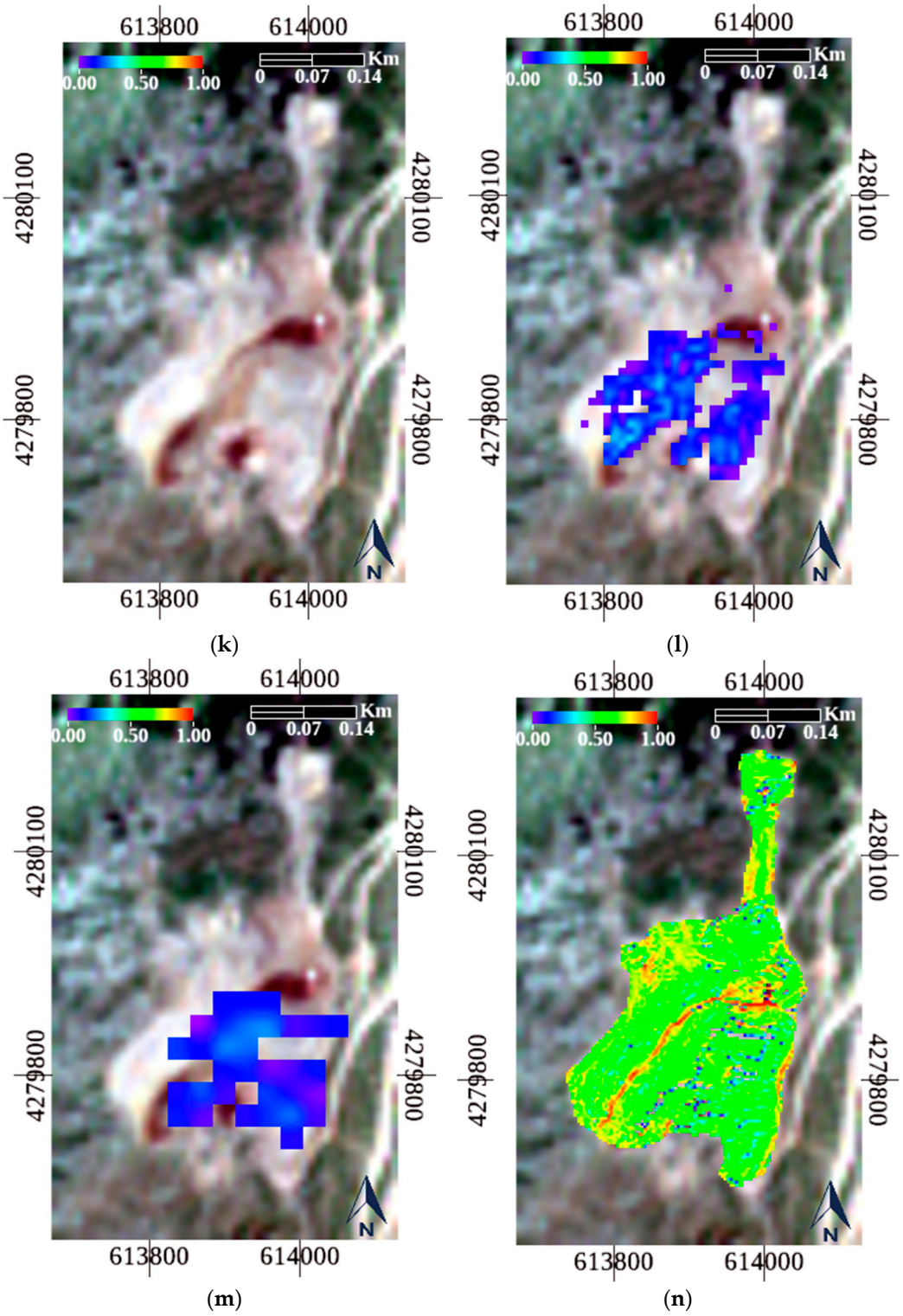


Figure 7. *Cont.*

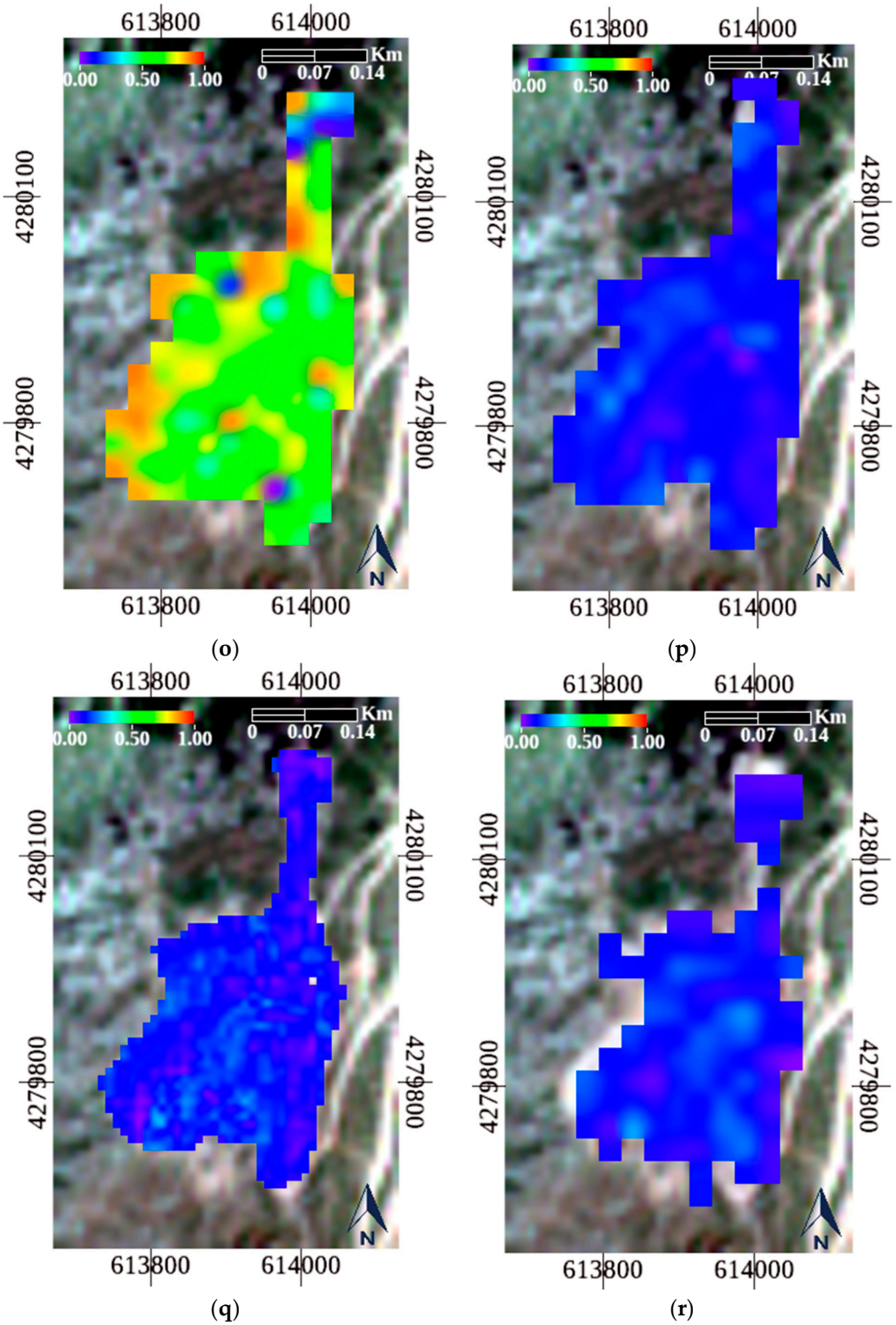


Figure 7. *Cont.*

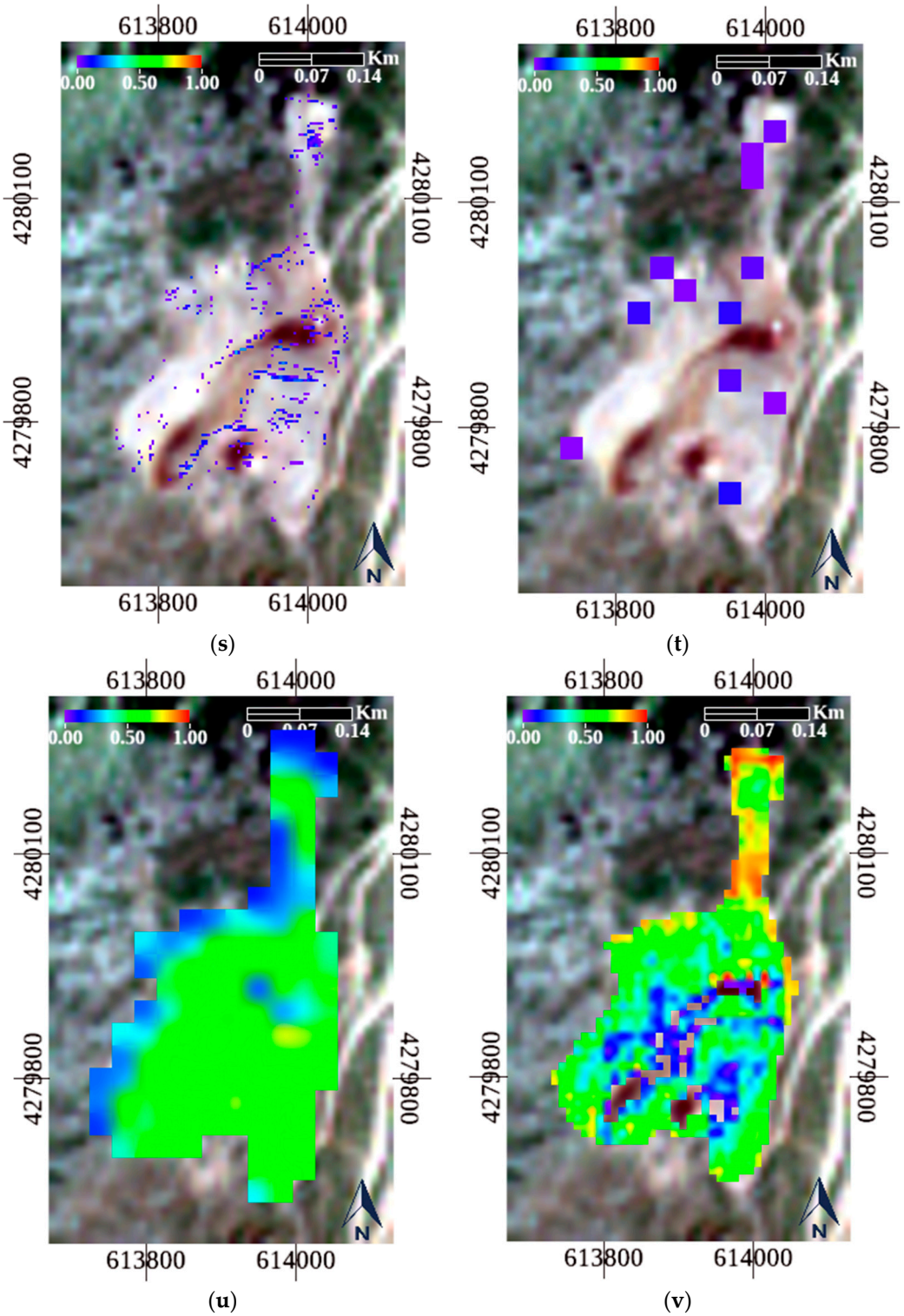


Figure 7. *Cont.*

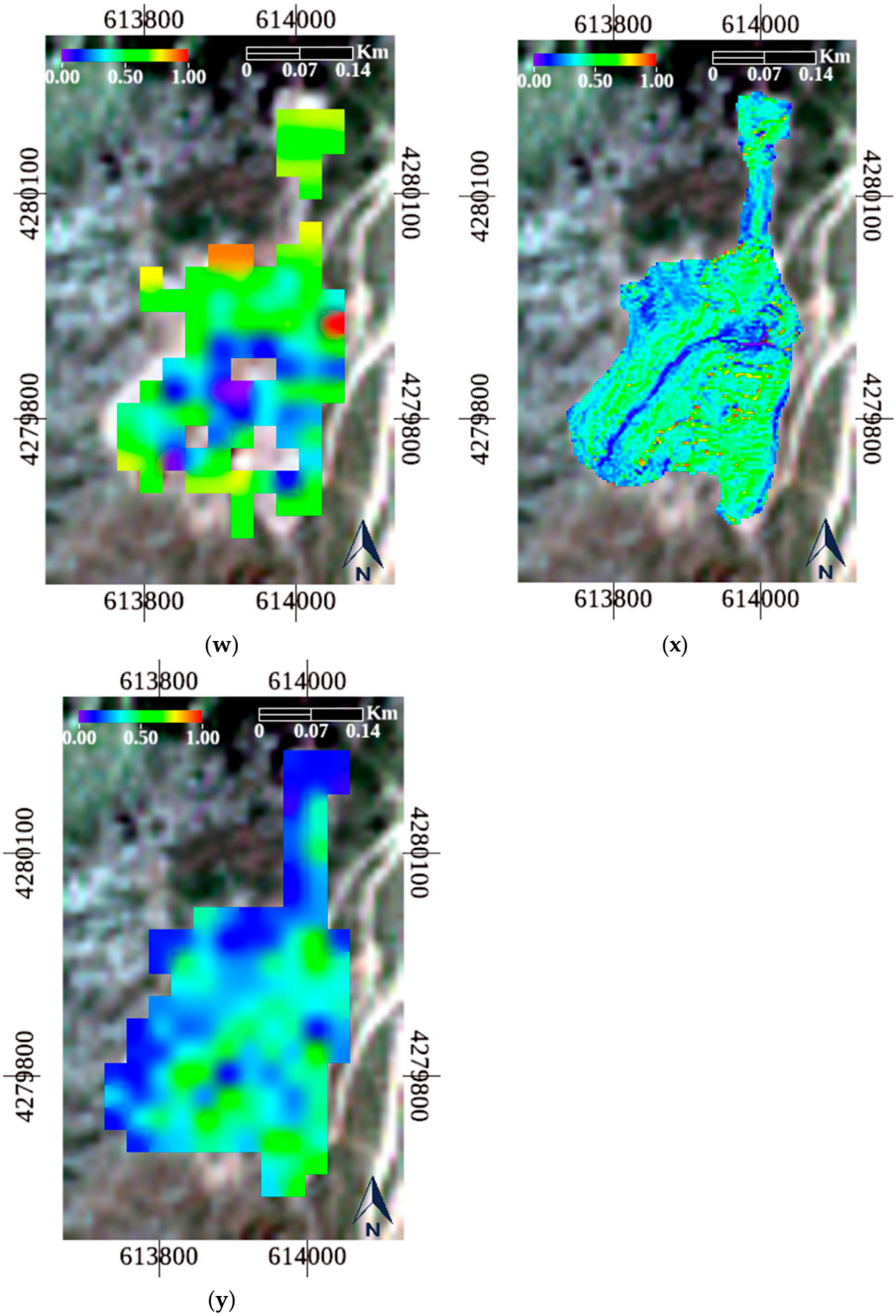


Figure 7. Abundance maps (from top to bottom) of hematite (**a**–**e**), goethite (**f**–**j**), anatase (**k**–**o**), kaolinite (**p**–**t**), and calcite (**u**–**y**). The first column corresponds to EnMap (30 m), the second and third columns to Sentinel-2 (10 m and 30 m), and the fourth and fifth columns to WV3-SWIR (3.7 m and 30 m). Endmembers are retrieved from the JPL spectral library. Abundance colors range from low, 0 (purple), to high, 1 (red), values. Basemap: the TCI of Sentinel-2 (26 June 2024).

Table 5. Summary of mineral mapping results: spatial distribution is given as low, moderate, and high for both methods. Endmembers are retrieved from the USGS spectral library.

Mineral	Sensor	Spatial Resolution (m)	SAM Spatial Distribution	LSU Spatial Distribution
AlOOH	EnMap	30	Moderate	Moderate
	Sentinel-2	10	High	High
	Sentinel-2	30	High	High
	WV3-SWIR	3.7	High	Moderate
	WV3-SWIR	30	High	Moderate
Hematite	EnMap	30	High	High
	Sentinel-2	10	High	High
	Sentinel-2	30	High	High
	WV3-SWIR	3.7	High	High
	WV3-SWIR	30	High	High
Goethite	EnMap	30	Moderate	High
	Sentinel-2	10	High	High
	Sentinel-2	30	High	High
	WV3-SWIR	3.7	-	-
	WV3-SWIR	30	-	-
Kaolinite	EnMap	30	Low	High
	Sentinel-2	10	High	High
	Sentinel-2	30	High	High
	WV3-SWIR	3.7	High	High
	WV3-SWIR	30	High	High
Calcite	EnMap	30	-	-
	Sentinel-2	10	High	Low
	Sentinel-2	30	High	Low
	WV3-SWIR	3.7	High	High
	WV3-SWIR	30	High	High

Table 6. Sensor-detected minerals and ground–satellite agreement at sixteen GCPs: ✓ represents detected, ✓? represents slightly detected, and × represents not detected. Mineral detection for each method in the classification/abundance image is provided in the SAM and LSU columns, respectively. Ground–satellite agreement at the 16 GCPs is shown in the SAM and LSU GCP columns, respectively; the number in parentheses indicates the quantity of common minerals. Endmembers are retrieved from the USGS spectral library.

Mineral	Sensor	Spectral Resolution (m)	SAM	LSU	SAM GCPs	LSU GCPs
AlOOH	EnMap	30	✓	✓?	✓ (2)	×
	Sentinel-2	10	✓	✓	✓ (7)	✓ (3)
	Sentinel-2	30	✓	✓	✓ (4)	✓ (4)
	WV3-SWIR	3.7	✓	✓?	✓ (8)	✓ (1)
	WV3-SWIR	30	✓	✓?	✓ (4)	✓ (1)

Table 6. *Cont.*

Mineral	Sensor	Spectral Resolution (m)	SAM	LSU	SAM GCPs	LSU GCPs
Hematite	EnMap	30	✓	✓	✓ (6)	✓ (6)
	Sentinel-2	10	✓	✓	✓ (8)	✓ (7)
	Sentinel-2	30	✓	✓	✓ (5)	✓ (6)
	WV3-SWIR	3.7	✓	✓	✓ (8)	✓ (9)
	WV3-SWIR	30	✓	✓	✓ (4)	✓ (3)
Goethite	EnMap	30	✓	✓	×	×
	Sentinel-2	10	✓	✓	×	×
	Sentinel-2	30	✓	✓	×	×
	WV3-SWIR	3.7	×	×	×	×
	WV3-SWIR	30	×	×	×	×
Kaolinite	EnMap	30	✓?	✓	✓ (2)	✓ (7)
	Sentinel-2	10	✓	✓?	✓ (7)	✓ (5)
	Sentinel-2	30	✓	✓?	✓ (7)	✓ (6)
	WV3-SWIR	3.7	✓	✓	✓ (10)	✓ (7)
	WV3-SWIR	30	✓	✓	✓ (5)	✓ (6)
Calcite	EnMap	30	×	×	×	×
	Sentinel-2	10	✓	✓?	✓ (11)	×
	Sentinel-2	30	✓	✓?	✓ (9)	×
	WV3-SWIR	3.7	✓	✓	✓ (10)	✓ (12)
	WV3-SWIR	30	✓	✓	✓ (5)	✓ (9)

Table 7. Summary of mineral mapping results: spatial distribution is given as low, moderate, and high for both methods. Endmembers are retrieved from the JPL spectral library.

Mineral	Sensor	Spatial Resolution (m)	SAM Spatial Distribution	LSU Spatial Distribution
Anatase	EnMap	30	Low	-
	Sentinel-2	10	High	Low
	Sentinel-2	30	High	Low
	WV3-SWIR	3.7	High	High
	WV3-SWIR	30	High	High
Hematite	EnMap	30	High	Low
	Sentinel-2	10	High	Low
	Sentinel-2	30	High	Low
	WV3-SWIR	3.7	High	-
	WV3-SWIR	30	High	Low

Table 7. *Cont.*

Mineral	Sensor	Spatial Resolution (m)	SAM Spatial Distribution	LSU Spatial Distribution
Goethite	EnMap	30	Moderate	High
	Sentinel-2	10	-	High
	Sentinel-2	30	-	High
	WV3-SWIR	3.7	High	-
	WV3-SWIR	30	High	-
Kaolinite	EnMap	30	Low	High
	Sentinel-2	10	High	High
	Sentinel-2	30	High	High
	WV3-SWIR	3.7	High	Low
	WV3-SWIR	30	High	Low
Calcite	EnMap	30	Moderate	High
	Sentinel-2	10	High	High
	Sentinel-2	30	High	High
	WV3-SWIR	3.7	High	High
	WV3-SWIR	30	High	High

Table 8. Sensor-detected minerals and ground–satellite agreement at the sixteen GCPs: ✓ represents detected, ✓? represents slightly detected, and × represents not detected. Mineral detection for each method in the classification/abundance image is provided in the SAM and LSU columns, respectively. Ground–satellite agreement at the 16 GCPs is shown in the SAM and LSU GCP columns, respectively; the number in parentheses indicates the quantity of common minerals. Endmembers are retrieved from the JPL spectral library.

Mineral	Sensor	Spectral Resolution (m)	SAM	LSU	SAM GCPs	LSU GCPs
Hematite	EnMap	30	✓	✓?	✓ (5)	×
	Sentinel-2	10	✓	✓?	✓ (8)	×
	Sentinel-2	30	✓	✓?	✓ (6)	✓ (1)
	WV3-SWIR	3.7	✓	✓?	✓ (8)	×
	WV3-SWIR	30	✓	✓?	✓ (4)	×
Goethite	EnMap	30	✓	✓	×	×
	Sentinel-2	10	×	✓	×	×
	Sentinel-2	30	×	✓	×	×
	WV3-SWIR	3.7	✓	×	×	×
	WV3-SWIR	30	✓	×	×	×
Anatase	EnMap	30	✓?	×	×	×
	Sentinel-2	10	✓?	×	✓ (6)	×
	Sentinel-2	30	✓?	×	✓ (4)	✓ (1)
	WV3-SWIR	3.7	✓	✓	✓ (7)	✓ (5)
	WV3-SWIR	30	✓	✓	✓ (4)	✓ (2)

Table 8. *Cont.*

Mineral	Sensor	Spectral Resolution (m)	SAM	LSU	SAM GCPs	LSU GCPs
Kaolinite	EnMap	30	✓?	✓	×	✓ (1)
	Sentinel-2	10	✓	✓	✓ (7)	✓ (8)
	Sentinel-2	30	✓	✓	✓ (7)	✓ (6)
	WV3-SWIR	3.7	✓	✓?	✓ (10)	×
	WV3-SWIR	30	✓	✓?	✓ (5)	×
Calcite	EnMap	30	✓	✓	✓ (7)	✓ (9)
	Sentinel-2	10	✓	✓	✓ (11)	✓ (10)
	Sentinel-2	30	✓	✓	✓ (9)	✓ (9)
	WV3-SWIR	3.7	✓	✓	✓ (12)	✓ (12)
	WV3-SWIR	30	✓	✓	✓ (7)	✓ (9)

3.2.1. USGS Spectral Library

SAM and LSU Results: Visual Interpretation

The five mineral classification maps generated are presented in Figures 4 and 5 (SAM and LSU, respectively). The rows depict the endmembers and the columns depict the sensors. From left to right, the mineral classification maps are presented in the spatial resolution of EnMap (30 m), Sentinel-2 (10 m), Sentinel-2 (30 m), WV3-SWIR (3.7 m), and WV3-SWIR (30 m), respectively. The angle threshold is defined as 0.25 radians and applies to all data. Figure 4 depicts the range of angles (0–0.25 radians) of SAM while Figure 5 depicts the relative abundances, with cold colors indicating lower values and warm colors indicating higher values.

AlOOH is consistently mapped with all sensors using SAM; however, LSU indicates low abundance, especially in EnMap, potentially due to its coarse (30 m) spatial resolution. Partial spatial coverage is shown with Sentinel-2 and WV3-SWIR data. We point out the high angles (Figure 4a) and the low abundances (Figure 5a) for the EnMap data, as well as the moderate to high angles with the low abundances of Sentinel-2 (10 m and 30 m) and WV3-SWIR (3.7 m and 30 m). AlOOH is detected by all sensors, and both methods are based on the visual interpretation.

Hematite: In describing the results across the sensors in relation to SAM and LSU, hematite is spatially mapped throughout the study area. We notice high to very high angles and low abundances in EnMap (Figures 4f and 5f), while Sentinel-2 (10 m and 30 m) presents moderate angles (Figure 4g,h) with low to moderate abundances (Figure 5g,h). In Sentinel-2, we also observe moderate angles at 10 m and 30 m spatial resolutions, while in most cases, the abundance values exhibit a subtle shift to lower abundances in Sentinel-2 (10 m) and higher abundances in Sentinel-2 (30 m). Hematite, as an iron oxide mineral, exhibits characteristic spectral absorption features in the VNIR spectral region, especially at 850–900 nm and 500–600 nm, which fall within the EnMap and Sentinel-2 spectral range, possibly explaining the reason that both sensors display a similar pattern for hematite. On the other hand, the WV3-SWIR maps hematite with very high angles (Figure 4i,j) and moderate abundances (Figure 5i,j). However, WV3-SWIR lacks the VNIR spectral bands, which makes hematite detection dependent on SWIR spectral bands that could be confused with OH-bearing minerals like diaspore. Hematite is detected by all sensors and methods based on visual interpretation. Since Sentinel-2 presents the lowest angle among EnMap

and WW3-SWIR in conjunction with moderate to high abundances, we indicate Sentinel-2 as a better option to map hematite, followed by EnMap, based on the visual interpretation.

Goethite follows the spatial pattern of hematite except for the WV3-SWIR data, where the mineral is not detected. The results obtained from the EnMap reveal very high angles (Figure 4k) and low to moderate abundance values (Figure 5k). The values derived from Sentinel-2 (10 m and 30 m) indicate the moderate angle value group is in conjunction with the moderate to very high abundance group. Neither the WV3-SWIR data nor the in situ sample analysis (XRD) provides evidence of goethite presence. The ground data does not confirm goethite with the XRD analysis, suggesting that the satellite-based detection reflects misclassification.

Kaolinite is sparsely detected in the EnMap image, whereas it is fully mapped in Sentinel-2 and WV3-SWIR with SAM. On the other hand, there is extensive spatial coverage over the sensors using LSU, even if the corresponding abundances are too low (less than 10%). In the EnMap and Sentinel-2 sensors (Figure 4p–r), kaolinite results reveal high angles and low abundances (Figure 5p–r), while in WV3-SWIR, kaolinite shows high angles (Figure 4s,t) with low abundances (Figure 5s,t). All sensors indicate high angles and low abundances, which potentially indicate the insufficient presence of kaolinite in the study area, something that is also indicated by the laboratory analysis results. Kaolinite is mapped with three sensors, and both methods are based on visual interpretation.

Calcite is present in all pixels in the case of SAM with the Sentinel-2 and WV3-SWIR data but not mapped with the EnMap sensor. When applying the LSU, a limited spatial coverage is observed for Sentinel-2; it is not mapped with EnMap but is present in all pixels of the WV3-SWIR image. The results, as retrieved from Sentinel-2 (10 m and 30 m), show high to very high angles (Figure 4v,w) and low abundance values (Figure 5v,w). Moderate to very high angles with low to high abundances are observed for the WV3-SWIR (10 m and 30 m) sensor. Calcite seems to be mapped better using WV3-SWIR (3.7 m and 30 m) compared to the other two sensors, a quality attributed to CO3, which has its absorption feature at (2300–2370 nm) [58].

Detection Capability of Satellite Sensors

Tables 5 and 6 present the results of mineral occurrence as derived from two different approaches (SAM and LSU) for each sensor (EnMap, Sentinel-2, and WV3-SWIR) across multiple spatial scales, retrieving endmembers from the USGS spectral library as well as the ground–satellite agreement based on the sixteen GCPs as a summary of the predicted presence of over-measurement.

Table 5 highlights the differences in minerals' spatial distribution, which is described in the "SAM and LSU results: Visual Interpretation" section.

Table 6 highlights differences in mineral detectability in relation to the sensor, spatial resolution, and spectral coverage when GCPs are used. Hematite is consistently detected by both methods across all data, with lesser deviation between SAM and LSU (we note 8/16 common points for Sentinel-2: (10 m) and 7/16 common points for LSU (10 m)). AlOOH shows more reliable detection with SAM than LSU; this material fails to be detected in EnMap but is more successfully mapped in Sentinel-2 (10 m) and WV3-SWIR (3.7 m). Kaolinite is also detected by both methods, and all data collected with WV3-SWIR present the most stable results (we note 10/16 common points for a WV3-SWIR 3.7 m sensor with SAM and 7/16 common points for LSU). Calcite is not detected in EnMap but is resolved in Sentinel-2 and especially in WV3-SWIR. Detection in WV3-SWIR (3.7 m) is achieved with both methods (SAM with 10/16 common points and 12/16 common points for LSU). In contrast, goethite is not detected with the ground data.

3.2.2. JPL Spectral Library

SAM and LSU Results: Visual Interpretation

The five mineral classification maps generated are presented in Figures 6 and 7 (SAM and LSU, respectively). The rows depict the endmembers and the columns depict the sensors. From left to right, the mineral classification maps are presented in the spatial resolution of EnMap 30 m, Sentinel-2 10 m, Sentinel-2 30 m, WV3-SWIR 3.7 m, and WV3-SWIR 30 m, respectively. The angle threshold is defined as 0.25 radians and applies to all data. Figure 6 depicts the range of SAM angles (0–0.25 radians), with cold colors indicating low angle values and warm colors indicating high angle values, while Figure 7 depicts the abundances, with warm colors denoting high abundance values.

Hematite is fully mapped by every sensor with SAM, while only a small part of the pixels is mapped with LSU. Very high angles (Figure 6a–e) are observed for EnMap and WV3-SWIR and moderate to high angles for Sentinel-2. By contrast, the LSU generates sparser mapping over a limited area for all sensors, with low to moderate abundances (Figure 7a–e). Hematite is mapped by all sensors, with Sentinel-2 having the lower angles, but is hardly mapped with the LSU. Goethite is spatially dominant using SAM with EnMap and WV3-SWIR, but it is not detected with Sentinel-2. It is also spatially dominant using LSU with EnMap and Sentinel-2, but it is not detected with WV3-SWIR. Very high angle values are present not only in EnMap but also in WV3-SWIR data (Figure 6f–j). Low to moderate abundances are recorded for EnMap, and similarly, low to moderate abundances are observed for Sentinel-2 (Figure 7f–h). The ground data does not confirm goethite with the XRD analysis, suggesting that satellite-based detection can reflect misclassification.

Anatase is spatially limited (almost absent) in EnMap data; nonetheless, it is spatially dominant in Sentinel-2 and WV3-SWIR based on SAM. It is not traceable with EnMap, it has moderate spatial coverage with Sentinel-2, and it has full spatial coverage with WV3-SWIR data and LSU. Concerning SAM, very high angles are observed in all sensors (Figure 6k–o), while low abundances (Figure 7k–m) are calculated for Sentinel-2 and moderate to high abundances for WV3-SWIR (Figure 7n,o). Although not anticipated, the WV3-SWIR spectral bands map high abundances; this can be explained by the fact that the anatase endmember in WV3-SWIR is almost featureless (Figure 2), leading to misclassification.

Kaolinite is limited in its spatial distribution using EnMap data, while it presents full spatial coverage in the case of SAM. By applying LSU, kaolinite is not mapped in EnMap; it covers the entire spatial area with the Sentinel-2 data, and it has a minimum spatial representation using WV3-SWIR. Very high angles are calculated for EnMap and Sentinel-2 and high angles for WV3-SWIR (Figure 6p–t). Low abundances (Figure 7p–t) are observed for all sensors. All sensors indicate high angles and low abundances, indicating the insufficient presence of kaolinite in the study area.

Calcite, either through the results from SAM or those from LSU, is characterized by full spatial coverage. Very high angles are observed in EnMap and moderate to high angles in Sentinel-2 and WV3-SWIR (Figure 6u–y). Moderate to high abundances are calculated for all sensors (Figure 7u–y). All sensors with both methods map calcite based on visual interpretation.

Detection Capability of Satellite Sensors

Tables 7 and 8 present the results of mineral occurrence as derived from the two different approaches (SAM and LSU) for each sensor (EnMap, Sentinel-2, and WV3-SWIR) across multiple spatial scales, retrieving endmembers from the JPL spectral library as well as the ground–satellite agreement based on the sixteen GCPs as a summary of the predicted presence of over-measurement.

Table 7 highlights the differences in minerals' spatial distribution, which is described in the "SAM and LSU results: Visual Interpretation" section.

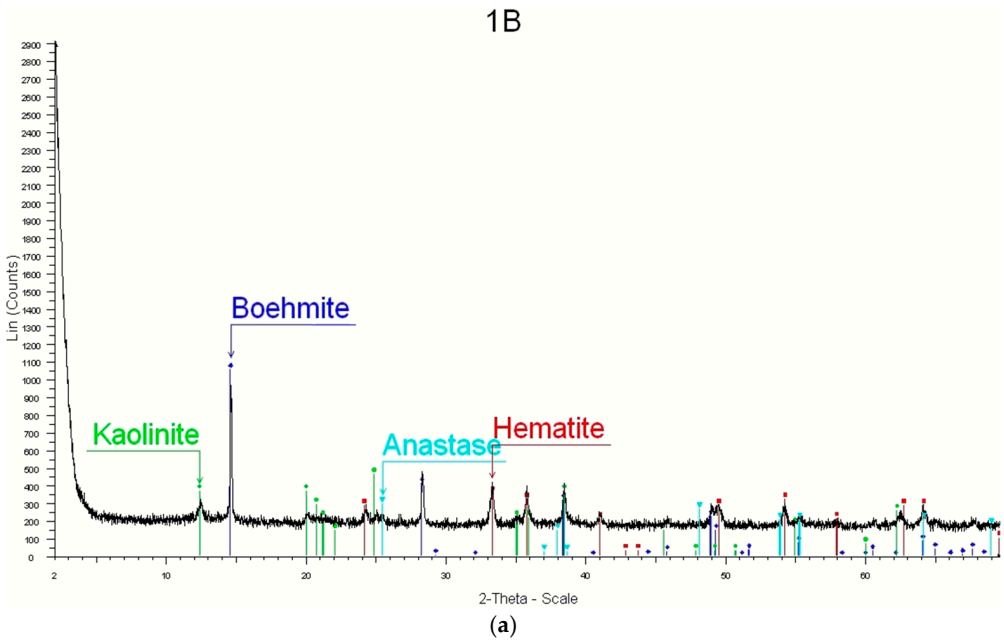
Table 8 highlights differences in mineral detectability in relation to the sensor, spatial resolution, and spectral coverage when GCPs are used.

Calcite is the most consistently detected mineral across all sensors and methods, with high-count GCPs for SAM and LSU (we note 12/16 common points for WV3-SWIR 3.7 m for the SAM and LSU). Hematite is consistently detected by the SAM method across all data but not with the LSU (we note 8/16 common points for Sentinel-2 10 m and 8/16 common points for WV3-SWIR 3.7 m for the SAM). Kaolinite is detected by both methods only for Sentinel-2 (we note 10/16 common points for WV3-SWIR 3.7 m and SAM). Anatase achieved the highest GCP counts for WV3-SWIR compared to other sensors; however, we believe that this is the result of misclassification. Finally, goethite is not detected with the ground data.

3.3. In Situ

Bulk XRF analysis shows that the dominant major oxides are Al_2O_3 and CaO, followed by Fe_2O_3, TiO_2, and SiO_2, with minor MgO (primarily in limestones) (Table 2). These results are consistent with the expected lithological and mineralogical characteristics reported in the literature [41,45,59].

When combined with XRD analysis results, the bulk geochemical results indicate that the bauxites are mainly composed of AlOOH, hematite, anatase, and kaolinite, whereas the limestones consist predominantly of calcite and minor dolomite. Both lithologies contain very small amounts of quartz. The mixed samples display a composition reflecting mixtures of their bauxite–limestone components. Loss on ignition (LOI) values are high, largely due to CO_2 released from the carbonate mineral fraction and, to a far lesser extent, due to structural water in clays. The clay mineral in our samples is identified through clay fraction experiments as kaolinite. Its characteristic peak collapsed at approximately 21° 2θ following thermal treatment, while ethylene glycol treatment produced no shift, consistent with kaolinite behavior (Figure 8c).



(**a**)

Figure 8. *Cont.*

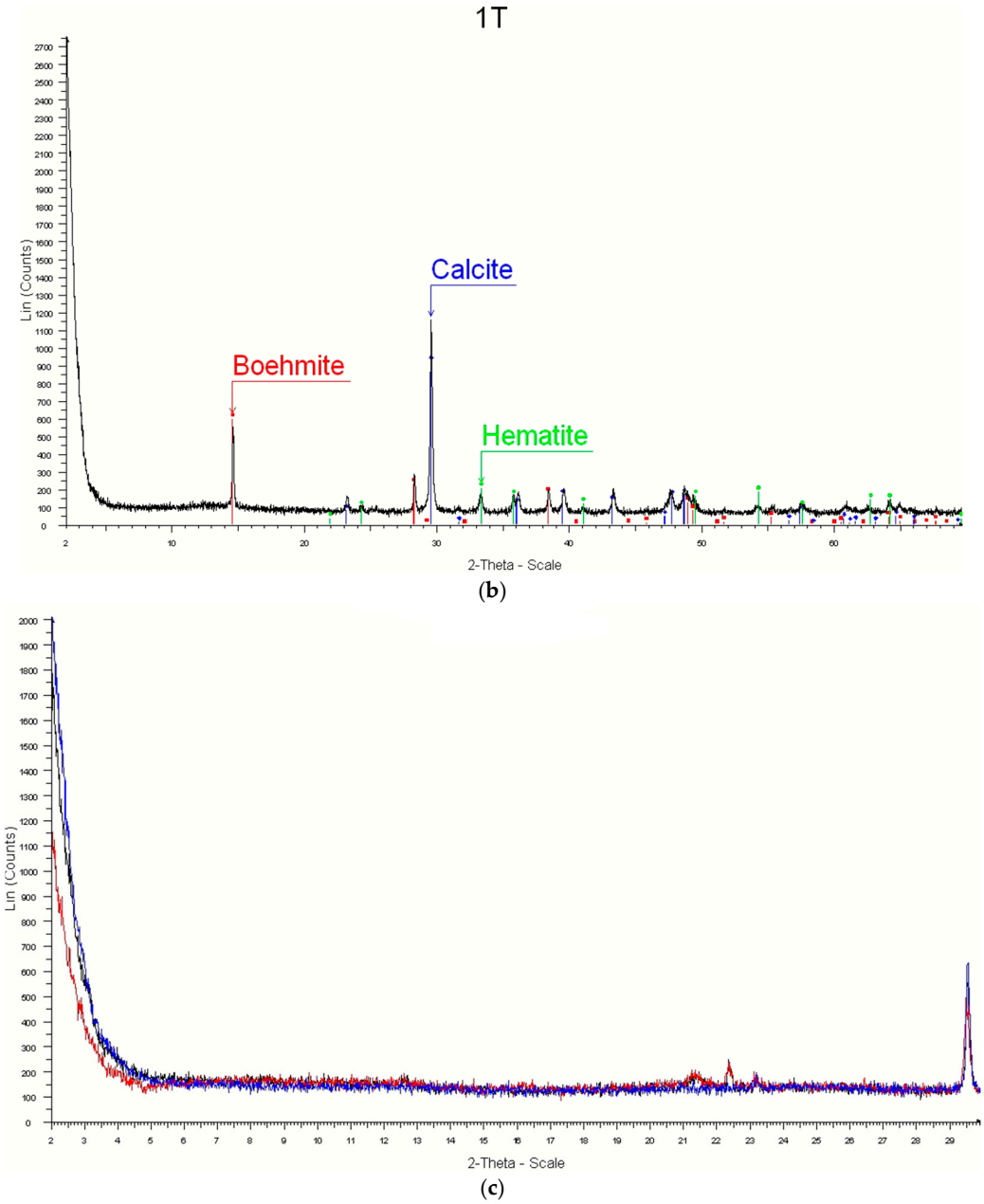


Figure 8. XRD graph of standard Arkoudotrypa bauxite, with (**a**) representing the sample code 1B, (**b**) representing the sample code 1T, and (**c**) representing the clay fraction separation experiment for standard Arkoudotrypa bauxite: black is unmodified bauxite, red is ethylene-glycol-treated bauxite, and blue is thermally treated bauxite.

3.4. Validation

The results described herein provide a foundation for evaluating the sensors' capability to map mine wastes within the methodological framework of this study. As outlined above, the validation procedure is based on mineral presence/absence and not on angle/abundance values. We concisely present the validation results with emphasis on the F1-score, which calculates the accuracy for each mineral class [57] based on the field data (XRD results) as a reference for the validation procedure (Tables 9 and 10).

The validation results highlight the F1-scores for AlOOH, hematite, anatase, kaolinite, and calcite across multiple remote sensing datasets. Goethite is not detected in the XRD analysis and is not validated using ground data. The validation results point out that the accuracy of each mineral mapping varies with both the data and the algorithm. We also

define high F1-score values as greater than 0.80, moderate F1-score values as between 0.60 and 0.80, and low F1-score values as less than 0.60.

Table 9. Validation results based on F1-score (×: validation results show no confirmed presence). Endmembers are retrieved from the USGS spectral library.

Mineral	EnMap (30 m) SAM	EnMap (30 m) LSU	Sentinel-2 (10 m) SAM	Sentinel-2 (10 m) LSU	Sentinel-2 (30 m) SAM	Sentinel-2 (30 m) LSU	WV3-SWIR (3.7 m) SAM	WV3-SWIR (3.7 m) LSU	WV3-SWIR (30 m) SAM	WV3-SWIR (30 m) LSU
AlOOH	0.57	×	0.78	0.57	0.62	0.73	0.80	0.20	0.80	0.33
Hematite	0.80	0.80	0.80	0.78	0.71	0.86	0.80	0.82	0.62	0.55
Kaolinite	0.50	0.88	0.74	0.67	0.88	0.80	0.87	0.76	0.83	0.86
Calcite	×	×	0.96	×	1.00	×	0.87	0.96	0.71	1.00

Table 10. Validation results based on F1-score (×: validation results show no confirmed presence). Endmembers are retrieved from the JPL spectral library.

Mineral	EnMap (30 m) SAM	EnMap (30 m) LSU	Sentinel-2 (10 m) SAM	Sentinel-2 (10 m) LSU	Sentinel-2 (30 m) SAM	Sentinel-2 (30 m) LSU	WV3-SWIR (3.7 m) SAM	WV3-SWIR (3.7 m) LSU	WV3-SWIR (30 m) SAM	WV3-SWIR (30 m) LSU
Anatase	×	×	0.67	×	0.62	0.33	0.78	0.56	0.62	0.50
Hematite	0.71	×	0.80	×	0.80	0.29	0.84	×	0.62	×
Kaolinite	×	0.25	0.74	0.89	0.88	0.80	0.87	×	0.83	×
Calcite	0.93	1.00	0.96	0.95	1.00	1.00	0.96	0.96	0.88	1.00

In a multiple-sensor system within the USGS endmembers, AlOOH shows a moderate performance across sensors and methods except with WV3-SWIR (0.80) using the SAM. The F1-score for hematite remains relatively high and stable (around 0.80) among the sensors and the methods, with the lowest value for WV3-SWIR (30 m) for both SAM and LSU (0.62 and 0.55, respectively), indicating that almost all sensors have the potential to capture the spectral pattern of the mineral, with EnMap and Sentinel-2 outperforming WV3-SWIR (30 m). Goethite is not validated since XRD does not indicate the presence of this mineral in the sampling locations. Kaolinite depicts similar scores except for EnMap with SAM (0.50) and Sentinel-2 (10 m) with both methods. It performs better on WV3-SWIR with both methods, reaching an F1-score up to 0.87, making this sensor more adequate to map kaolinite. Only with WV3-SWIR and both methods is a high F1-score achieved, indicating consistency among the methods and making WV3-SWIR suitable for mapping calcite.

In most cases, LSU results are not validated due to the limited or absent occurrence of the respective minerals in the study area. Hematite shows a high F1-score (0.80) in Sentinel-2 using SAM and (0.84) in WV3-SWIR, indicating that WV3-SWIR with SAM performs slightly better than Sentinel-2 in terms of F1-scores. However, it should be noted that these F1-scores are based on mineral absence/presence rather than on angle/abundance values. Goethite is not validated given the absence of in situ data. Anatase shows inconsistent behavior: if and where the F1-scores are calculated, they yield low to moderate scores (0.33 to 0.78), indicating that neither sensor can reliably map the anatase with these methods. Even if kaolinite does not belong to the main phase, high F1-scores for Sentinel-2 (0.74 and 0.88) and WV3-SWIR (0.87 and 0.83) are obtained using SAM. Finally, calcite achieves high F1-scores in mineral detection for every sensor with both methods.

4. Discussion

We have already discussed in detail the similarities and the differences in the mineral mapping of bauxite mine wastes using multiple sensors with different spatial scales using the visual interpretation and validation in the Section 3. The goal of this study is to evaluate the accuracy of the methodology in mapping these minerals and highlight the best sensors/methods (highlight trade-offs among spatial and spectral resolution and method sensitivity, which have not explicitly addressed earlier by combining the above parameters).

Our processing methodology is in full accordance with previous studies, as the two classification methodologies (SAM and LSU) and the petrographic and geochemical analyses (XRF, XRD, and LA-ICP-MS) have been used in previous studies. SAM is evaluated as a classifier in multispectral data [2,17,19,25] or in both multispectral and hyperspectral data [18]. LSU is also applied to multispectral [28,29] or hyperspectral [60] data for mineral detection and mapping. In the same way, XRF, XRD, and LA-ICP-MS are the most common laboratory analyses performed on field samples [13,18,61].

The validation results based on F1-scores prove that generally the USGS spectral library presents higher scores in comparison with JPL. It is characteristic that hematite is detected in all the sensors independently of the spatial resolution (3.7 m to 30 m) and the classifier (SAM or LSU) when the USGS spectral signature is used. On the contrary, the JPL (spectral signature) and LSU classifier combination fail to detect hematite. The same result is retrieved for the kaolinite classification. This is in accordance with previous studies [49].

The comparison between multispectral and hyperspectral sensors for mineral mapping conducted in this study is consistent with previous research [11,19,62]. However, for the first time, the spatial resolution of the data is deliberately degraded, and its effect on the classification procedure is systematically evaluated and validated. The spatial resolution downsampling applied to Sentinel-2 and WW3 data proves that the spectral resolution remains the dominant factor in the classification procedure. It is worth mentioning that the minerals identified in the original data (Sentinel-2 at 10 m and WV3-SWIR at 3.7 m) are also detected after the spatial downsampling at 30 m. However, a slight decrease in F1-score (Tables 9 and 10) is observed for hematite detection in both Sentinel-2 and WV3-SWIR data following downsampling from 10 m and 3.7 m to 30 m, respectively, indicating a modest impact of reduced spatial resolution.

It is also notable that WV3-SWIR bands effectively map calcite in both the original (3.7 m) and the downsampled (30 m) spatial resolution. This is due to its narrow, well-positioned SWIR bands that capture the diagnostic carbonate absorption feature near 2.33–2.35 μm.

Sentinel-2 seems to present a slightly higher detectability for iron oxides (e.g., hematite) as presented in Tables 9 and 10, despite the lower spectral resolution. This is acceptable because iron oxides exhibit broad, high-contrast spectral features that can be effectively captured without hyperspectral resolution. Sentinel-2′s well-placed VNIR and Red-Edge bands align with key iron oxide absorption features, while its finer spatial resolution (10 m) reduces spectral mixing on heterogeneous surfaces. In addition, Sentinel-2 benefits from high signal-to-noise ratios and radiometric stability in the VNIR region, where iron oxide signatures are strongest, allowing spatial resolution and data robustness to outweigh the advantages of EnMap's higher spectral resolution.

Both classification techniques used in this study (SAM and LSU) are well-established and extensively documented in the literature [18–20,29,31,60,61]. In principle, their applicability depends on the spectral and spatial characteristics of the sensor and the selection of representative endmembers. Both methods primarily rely on absorption band position and depth, assume fixed endmember spectra, and are sensitive to factors such as grain size, degree of mixing, and illumination conditions; consequently, classification uncertainties

may arise when diagnostic absorption features are slightly shifted or superimposed in satellite observations. In this case study, SAM outperforms LSU for most detected minerals (Tables 9 and 10), which is attributed to differences in endmember purity and grain-size effects. For nearly all minerals and sensors, higher F1-scores are obtained using SAM, with kaolinite (Table 10) being the only exception, where LSU achieves better detectability. Although the use of field spectra could potentially improve the representation of local mineralogy and refine the LSU results, this approach is beyond the scope of the present study.

Finally, it is worth noting that goethite is identified in the Sentinel-2 and EnMap classifications but is not confirmed by geochemical analyses of the ground samples. This discrepancy may reflect either a false positive classification or limitations related to the spatial distribution and representativeness of the collected samples. Resolving this issue would require a targeted field campaign with sample collection at specific locations where goethite was detected through remote sensing.

The misclassification may have occurred because goethite (FeO(OH)) and hematite (Fe_2O_3) share similar ferric iron (Fe^{3+}) electronic absorption features, particularly in the visible near-infrared (VNIR) region. Both minerals exhibit strong absorptions and diagnostic spectral slopes related to Fe^{3+} crystal field transitions, which can overlap when observed at the spectral resolution of multispectral or even hyperspectral satellite sensors as presented in three previous studies [63–65]. As a result, their spectral signatures may appear very similar, especially when absorption features are broad, shallow, or affected by noise. In addition, grain size, crystallinity, and hydration state strongly influence the spectral response of iron oxides. Fine-grained or poorly crystalline hematite can exhibit goethite-like spectral characteristics, while dehydrated goethite can resemble hematite spectrally. These effects are amplified at the satellite scale, where mixed pixels and surface coatings dominate the observed signal.

5. Conclusions

This work aims to assess the effects of spatial and spectral resolution of EnMap, Sentinel-2, and WV3-SWIR using two different methods, SAM and LSU, with USGS- and JPL-retrieved endmembers on mapping bauxite mine waste. We compare results across sensors and validate them using the XRD results, highlighting each sensor's capabilities and limitations.

This study points out that mineral mapping accuracy in bauxite mining wastes is primarily controlled by spectral resolution and spectral coverage rather than spatial resolution.

Among the tested approaches, SAM outperforms LSU, particularly with USGS endmembers, yielding the highest satellite–ground agreement and F1-scores.

Hematite is detected across all sensors and scales, indicating it as a reliable indicator mineral, while kaolinite and calcite indicate a stronger sensitivity to the sensor–method combination.

Spatial downsampling confirms that minerals detected in fine resolution also remain identifiable in coarser spatial resolution, indicating that spectral information is preserved. Overall, these results highlight trade-offs between spatial and spectral characteristics, as well as the methodological approach supporting a multisensor and multiscale approach for optimization of the mineral map.

The findings underline the importance of selecting appropriate sensor–method combinations depending on the target minerals and highlight the potential of remote sensing as a cost-effective and scalable tool for environmental monitoring and sustainable mine site management.

6. Future Directions

Since the F1-score slightly deviates after resampling datasets to 30 m spatial resolution, it is proposed to examine the application of continuum removal to spectral bands encompassing only specific mineral-related diagnostic absorption bands in future work. In addition to this, the selection of specific bands to apply to LSU would be an interesting option (mainly to EnMap data) to tested. A target field campaign could give a clearer answer to the question of why goethite is mapped by satellite data and not detected by the XRD.

Author Contributions: Conceptualization, K.G.N., O.S. and H.T.; methodology, E.K., I.P. and K.G.N.; software, E.K. and I.P.; validation, E.K. and I.P.; formal analysis, E.K. and I.P.; investigation, E.K. and I.P.; resources, E.K., I.P., K.G.N., O.S. and H.T.; data curation, E.K. and I.P.; writing—original draft preparation, E.K. and I.P.; writing—review and editing, K.G.N., O.S. and H.T.; visualization, E.K. and I.P.; supervision, K.G.N., O.S. and H.T.; project administration, K.G.N.; funding acquisition, K.G.N. All authors have read and agreed to the published version of the manuscript.

Funding: This research is funded by the EUROPEAN UNION's HORIZON EUROPE programme, grant number ID 101091462", in the frame of the "m4mining project".

Data Availability Statement: EnMap data was provided by GFZ in the frame of the m4mining project, WV3-SWIR was provided by ESA, Sentinel-2 data are available at https://dataspace.copernicus.eu (accessed on 1 June 2024).

Acknowledgments: We are thankful to the European Space Agency (ESA) for providing, free of charge, the WV3-SWIR (2024/01/06) data under the accepted project proposal PP0094982—m4mining "Multiscale and Multisensor Remote Sensing Data processing for Mine tailing management"—Case study sites in Greece and in the Republic of Cyprus. We acknowledge that Sentinel-2 Level 2A images were downloaded from the European Space Agency: Copernicus Data Space Ecosystem. https://dataspace.copernicus.eu.

Conflicts of Interest: The authors declare no conflicts of interest.

References

1. Anifadi, A.; Sykioti, O.; Koutroumbas, K.; Vassilakis, E.; Vasilatos, C.; Georgiou, E. Discrimination of Fe-Ni-Laterites from Bauxites Using a Novel Support Vector Machines-Based Methodology on Sentinel-2 Data. *Remote Sens.* **2024**, *16*, 2295. [CrossRef]
2. Mujabar, P.S.; Dajkumar, S. Mapping of Bauxite Mineral Deposits in the Northern Region of Saudi Arabia by Using Advanced Spaceborne Thermal Emission and Reflection Radiometer Satellite Data. *Geo-Spat. Inf. Sci.* **2019**, *22*, 35–44. [CrossRef]
3. Turan, T.İ.; Diker, C. Remote Sensing of Listvenite Rock for Kaymaz Gold Deposit, Eskişehir-TÜRKİYE. *J. Geochem. Explor.* **2022**, *243*, 107110. [CrossRef]
4. Guglietta, D.; Conte, A.M.; Paciucci, M.; Passeri, D.; Trapasso, F.; Salvatori, R. Mining Residues Characterization and Sentinel-2A Mapping for the Valorization and Efficient Resource Use by Multidisciplinary Strategy. *Minerals* **2022**, *12*, 617. [CrossRef]
5. Cardoso-Fernandes, J.; Teodoro, A.C.; Lima, A. Remote Sensing Data in Lithium (Li) Exploration: A New Approach for the Detection of Li-Bearing Pegmatites. *Int. J. Appl. Earth Obs. Geoinf.* **2019**, *76*, 10–25. [CrossRef]
6. Amer, R.; El Mezayen, A.; Hasanein, M. ASTER Spectral Analysis for Alteration Minerals Associated with Gold Mineralization. *Ore Geol. Rev.* **2016**, *75*, 239–251. [CrossRef]
7. Bouzidi, W.; Mezned, N.; Abdeljaoued, S. Mineralogical Mapping Using EO-1 Hyperion Data for Iron Mine Identification. *J. Appl. Remote Sens.* **2022**, *16*, 024514. [CrossRef]
8. Kayet, N.; Pathak, K.; Chakrabarty, A.; Sahoo, S. Mapping the Distribution of Iron Ore Minerals and Spatial Correlation with Environmental Variables in Hilltop Mining Areas. *Environ. Earth Sci.* **2018**, *77*, 308. [CrossRef]
9. Davies, G.E.; Calvin, W.M. Mapping Acidic Mine Waste with Seasonal Airborne Hyperspectral Imagery at Varying Spatial Scales. *Environ. Earth Sci.* **2017**, *76*, 432. [CrossRef]
10. Ahumada-Mexía, R.; Murillo-Jiménez, J.M.; Ortega-Rubio, A.; Marmolejo-Rodríguez, A.J.; Nava-Sánchez, E.H. Identification of Mining Waste Using Remote Sensing Technique: A Case Study in El Triunfo Town, BCS, México. *Remote Sens. Appl. Soc. Environ.* **2021**, *22*, 100493. [CrossRef]

11. Orynbassarova, E.; Ahmadi, H.; Pour, A.B.; Yerzhankyzy, A.; Zakariya, M.; Omirzhanova, Z. PRISMA Hyperspectral Satellite Imagery for Mapping Alteration Minerals and Zones in Aktogay Porphyry Copper Deposit, Kazakhstan: Implications for New Discoveries. *Geocarto Int.* **2025**, *40*, 2591763. [CrossRef]
12. Gemusse, U.; Cardoso-Fernandes, J.; Lima, A.; Teodoro, A. Identification of Pegmatites Zones in Muiane and Naipa (Mozambique) from Sentinel-2 Images, Using Band Combinations, Band Ratios, PCA and Supervised Classification. *Remote Sens. Appl. Soc. Environ.* **2023**, *32*, 101022. [CrossRef]
13. Hoseinzade, Z.; Saremi, M.; Shojaei, M.; Mokhtari, A.R.; Beiranvand Pour, A.; Mirzabozorg, S.A.A.S.; Hezarkhani, A.; Maghsoudi, A.; Yousefi, S. Fusion of Remote Sensing and Geochemical Data Using Hybrid Variational Autoencoder- BIRCH Deep Learning Algorithm for Copper Prospectivity Mapping. *Remote Sens. Appl. Soc. Environ.* **2025**, *40*, 101738. [CrossRef]
14. Hubbard, B.E.; Gallegos, T.J.; Stengel, V. Mapping Abandoned Uranium Mine Features Using Worldview-3 Imagery in Portions of Karnes, Atascosa and Live Oak Counties, Texas. *Minerals* **2023**, *13*, 839. [CrossRef]
15. Bahrami, H.; Esmaeili, P.; Homayouni, S.; Pour, A.B.; Chokmani, K.; Bahroudi, A. Machine Learning-Based Lithological Mapping from ASTER Remote-Sensing Imagery. *Minerals* **2024**, *14*, 202. [CrossRef]
16. Hajaj, S.; El Harti, A.; Pour, A.B.; Khandouch, Y.; Fels, A.E.A.E.; Elhag, A.B.; Ghazouani, N.; Ustuner, M.; Laamrani, A. Evaluation of Heterogeneous Ensemble Learning Algorithms for Lithological Mapping Using EnMAP Hyperspectral Data: Implications for Mineral Exploration in Mountainous Region. *Minerals* **2025**, *15*, 833. [CrossRef]
17. Chniouar, M.; Wafik, A.; Daafi, Y.; Guglietta, D. Integrated Remote Sensing for Geological and Mineralogical Mapping of Pb-Zn Deposits: A Case Study of Jbel Bou Dahar Region Using Multi-Sensor Imagery. *Mining* **2024**, *4*, 302–325. [CrossRef]
18. Khurram, S.; Khalil Rao, Z.; Beiranvand Pour, A.; Riaz, K.; Fatima, A.; Ahmed, A. ASTER and Hyperion Satellite Remote Sensing Data for Lithological Mapping and Mineral Exploration in Ophiolitic Zones: A Case Study from Lasbela, Baluchistan, Pakistan. *Mining* **2025**, *5*, 53. [CrossRef]
19. Ng-Cutipa, W.L.; Lobato, A.; González, F.J.; Georgalas, G.P.; Zananiri, I.; Carvalho, M.; Cardoso-Fernandes, J.; Somoza, L.; Piña, R.; Lunar, R.; et al. Spectral Angle Mapper Application Using Sentinel-2 in Coastal Placer Deposits in Vigo Estuary, Northwest Spain. *Remote Sens.* **2025**, *17*, 1824. [CrossRef]
20. Anifadi, A.; Sykioti, O.; Koutroumbas, K.; Vassilakis, E. A Novel Spectral Index for Identifying Ferronickel (Fe–Ni) Laterites from Sentinel 2 Satellite Data. *Nat. Resour. Res.* **2022**, *31*, 1203–1224. [CrossRef]
21. Kasmaeeyazdi, S.; Mandanici, E.; Balomenos, E.; Tinti, F.; Bonduà, S.; Bruno, R. Mapping of Aluminum Concentration in Bauxite Mining Residues Using Sentinel-2 Imagery. *Remote Sens.* **2021**, *13*, 1517. [CrossRef]
22. Guglietta, D.; Belardi, G.; Passeri, D.; Salvatori, R.; Ubaldini, S.; Casentini, B.; Trapasso, F. Optimising the Management of Mining Waste by Means Sentinel-2 Imagery: A Case Study in Joda West Iron and Manganese Mine (India). *J. Sustain. Min.* **2020**, *19*, 4–32. [CrossRef]
23. Park, H.; Choi, J. Mineral Detection Using Sharpened VNIR and SWIR Bands of Worldview-3 Satellite Imagery. *Sustainability* **2021**, *13*, 5518. [CrossRef]
24. Rodríguez-Hernández, A.; Briones-Gallardo, R.; Razo, I.; Noyola-Medrano, C.; Lázaro, I. Processing Methodology Based on ASTER Data for Mapping Mine Waste Dumps in a Semiarid Polysulphide Mine District. *Can. J. Remote Sens.* **2016**, *42*, 643–655. [CrossRef]
25. Seifi, A.; Hosseinjanizadeh, M.; Ranjbar, H.; Honarmand, M. Identification of Acid Mine Drainage Potential Using Sentinel 2a Imagery and Field Data. *Mine Water Environ.* **2019**, *38*, 707–717. [CrossRef]
26. Abay, H.H.; Legesse, D.; Venkata Suryabhagavan, K.; Atnafu, B. Mapping of Ferric (Fe^{3+}) and Ferrous (Fe^{2+}) Iron Oxides Distribution Using ASTER and Landsat 8 OLI Data, in Negash Lateritic Iron Deposit, Northern Ethiopia. *Geol. Ecol. Landsc.* **2024**, *8*, 223–240. [CrossRef]
27. Sekandari, M.; Masoumi, I.; Pour, A.B.; Muslim, A.M.; Hossain, M.S.; Misra, A. ASTER and WorldView-3 Satellite Data for Mapping Lithology and Alteration Minerals Associated with Pb-Zn Mineralization. *Geocarto Int.* **2022**, *37*, 1782–1812. [CrossRef]
28. Tompolidi, A.-M.; Sykioti, O.; Koutroumbas, K.; Parcharidis, I. Spectral Unmixing for Mapping a Hydrothermal Field in a Volcanic Environment Applied on ASTER, Landsat-8/OLI, and Sentinel-2 MSI Satellite Multispectral Data: The Nisyros (Greece) Case Study. *Remote Sens.* **2020**, *12*, 4180. [CrossRef]
29. Mezned, N.; Dkhala, B.; Abdeljaouad, S. Multitemporal and Multisensory Landsat ETM+ and OLI 8 Data for Mine Waste Change Detection in Northern Tunisia. *J. Spat. Sci.* **2018**, *63*, 135–153. [CrossRef]
30. Pour, A.B.; Hashim, M. Alteration Mineral Mapping Using ETM+ and Hyperion Remote Sensing Data at Bau Gold Field, Sarawak, Malaysia. *IOP Conf. Ser. Earth Environ. Sci.* **2014**, *18*, 012149. [CrossRef]
31. Pour, A.B.; Hashim, M.; Van Genderen, J. Detection of Hydrothermal Alteration Zones in a Tropical Region Using Satellite Remote Sensing Data: Bau Goldfield, Sarawak, Malaysia. *Ore Geol. Rev.* **2013**, *54*, 181–196. [CrossRef]
32. Kruse, F.A.; Lefkoff, A.B.; Boardman, J.W.; Heidebrecht, K.B.; Shapiro, A.T.; Barloon, P.J.; Goetz, A.F.H. The Spectral Image Processing System (SIPS)—Interactive Visualization and Analysis of Imaging Spectrometer Data. *Remote Sens. Environ.* **1993**, *44*, 145–163. [CrossRef]

33. Magendran, T.; Sanjeevi, S. Hyperion Image Analysis and Linear Spectral Unmixing to Evaluate the Grades of Iron Ores in Parts of Noamundi, Eastern India. *Int. J. Appl. Earth Obs. Geoinf.* **2014**, *26*, 413–426. [CrossRef]
34. Kokaly, R.F.; Clark, R.N.; Swayze, G.A.; Livo, K.E.; Hoefen, T.M.; Pearson, N.C.; Wise, R.A.; Benzel, W.; Lowers, H.A.; Driscoll, R.L.; et al. *USGS Spectral Library Version 7*; U.S. Geological Survey: Reston, VA, USA, 2017.
35. JPL Spectral Library. Available online: https://speclib.jpl.nasa.gov/documents/jpl_desc (accessed on 13 November 2025).
36. Kalaitzidis, S.; Siavalas, G.; Skarpelis, N.; Araujo, C.V.; Christanis, K. Late Cretaceous Coal Overlying Karstic Bauxite Deposits in the Parnassus-Ghiona Unit, Central Greece: Coal Characteristics and Depositional Environment. *Int. J. Coal Geol.* **2010**, *81*, 211–226. [CrossRef]
37. Petrascheck, W.E. The Genesis of Allochthonous Karst-Type Bauxite Deposits of Southern Europe. *Miner. Depos.* **1989**, *24*, 77–81. [CrossRef]
38. Valeton, I.; Biermann, M.; Reche, R.; Rosenberg, F. Genesis of Nickel Laterites and Bauxites in Greece during the Jurassic and Cretaceous, and Their Relation to Ultrabasic Parent Rocks. *Ore Geol. Rev.* **1987**, *2*, 359–404. [CrossRef]
39. Aronis, G.A. Geographical distribution, geological placing and aspects on the genesis of the greek bauxite. *Bull. Geol. Soc. Greece* **1954**, *2*, 55–79.
40. Carras, N. La posizione stratigrafica dei calcari ad ellipsactinie Nella Zona del Parnasso. *Lab. Géologie L'université Athenai Greece* **1989**, *34*, 65–75.
41. Damoulianou, M.-E.; Kalaitzidis, S.; Pasadakis, N. Turonian-Senonian Organic-Rich Sedimentary Strata and Coal Facies in Parnassos-Ghiona Unit, Central Greece: An Assessment of Palaeoenvironmental Setting and Hydrocarbon Generation Potential. *Int. J. Coal Geol.* **2022**, *258*, 104029. [CrossRef]
42. Eliopoulos, D.G.; Economou-Eliopoulos, M. Geochemical and Mineralogical Characteristics of Fe–Ni- and Bauxitic-Laterite Deposits of Greece. *Ore Geol. Rev.* **2000**, *16*, 41–58. [CrossRef]
43. Bardossy, G. *Karst Bauxites, Bauxite Deposits on Carbonate Rocks, Developments in Economic Geology*; Elsevier: Amsterdam, The Netherlands, 1982; Volume 14, p. 441. [CrossRef]
44. Valeton, I. *Bauxites*; Developments in Soil Science; Elsevier: Amsterdam, The Netherlands; New York, NY, USA, 1972; ISBN 978-0-444-40888-4.
45. Mondillo, N.; Di Nuzzo, M.; Kalaitzidis, S.; Boni, M.; Santoro, L.; Balassone, G. Petrographic and Geochemical Features of the B3 Bauxite Horizon (Cenomanian-Turonian) in the Parnassos-Ghiona Area: A Contribution towards the Genesis of the Greek Karst Bauxites. *Ore Geol. Rev.* **2022**, *143*, 104759. [CrossRef]
46. Robertson, A.H.F. Late Palaeozoic–Cenozoic Tectonic Development of Greece and Albania in the Context of Alternative Reconstructions of Tethys in the Eastern Mediterranean Region. *Int. Geol. Rev.* **2012**, *54*, 373–454. [CrossRef]
47. EnMAP. Available online: https://www.enmap.org/ (accessed on 22 October 2025).
48. Copernicus Browser. Available online: https://browser.dataspace.copernicus.eu/ (accessed on 31 October 2025).
49. Kouzeli, E.; Nikolakopoulos, K.; Sykioti, O.; Asadzadeh, S.; Koerting, F.; Schläpfer, D. Satellite Imagery for Bauxite Mine Waste Mapping in the Frame of the M4mining Project. *Int. Arch. Photogramm. Remote Sens. Spat. Inf. Sci.* **2025**, *48*, 113–120. [CrossRef]
50. Meerdink, S.K.; Hook, S.J.; Roberts, D.A.; Abbott, E.A. The ECOSTRESS Spectral Library Version 1.0. *Remote Sens. Environ.* **2019**, *230*, 111196. [CrossRef]
51. Baldridge, A.M.; Hook, S.J.; Grove, C.I.; Rivera, G. The ASTER Spectral Library Version 2.0. *Remote Sens. Environ.* **2009**, *113*, 711–715. [CrossRef]
52. Sykioti, O.; Ganas, A.; Vasilatos, C.; Kypritidou, Z. Investigating the Capability of Sentinel-2 and Worldview-3 VNIR Satellite Data to Detect Mineralized Zones at an Igneous Intrusion in the Koutala Islet (Lavreotiki, Greece) Using Laboratory Mineralogical Analysis, Reflectance Spectroscopy and Spectral Indices. *Bull. Geol. Soc. Greece* **2023**, *59*, 175–213. [CrossRef]
53. Linear Spectral Unmixing. Available online: https://www.nv5geospatialsoftware.com/docs/LinearSpectralUnmixing.html (accessed on 22 December 2025).
54. Bedini, E. Application of WorldView-3 Imagery and ASTER TIR Data to Map Alteration Minerals Associated with the Rodalquilar Gold Deposits, Southeast Spain. *Adv. Space Res.* **2019**, *63*, 3346–3357. [CrossRef]
55. Fahmy Amin, M. Confusion Matrix in Binary Classification Problems: A Step-by-Step Tutorial. *J. Eng. Res.* **2022**, *6*. [CrossRef]
56. Fahmy Amin, M. Confusion Matrix in Three-Class Classification Problems: A Step-by-Step Tutorial. *J. Eng. Res.* **2023**, *7*. [CrossRef]
57. Xi, Y.; Mohamed Taha, A.M.; Hu, A.; Liu, X. Accuracy Comparison of Various Remote Sensing Data in Lithological Classification Based on Random Forest Algorithm. *Geocarto Int.* **2022**, *37*, 14451–14479. [CrossRef]
58. Geologically Based Spectral Analysis Guides for Mineral Exploration (GMEX)—Spectral Interpretation Field. Available online: https://pdfcoffee.com/gmex-spectral-interpretation-field-manual-pdf-pdf-free.html (accessed on 3 October 2025).
59. Laskou, M.; Economou-Eliopoulos, M. The Role of Microorganisms on the Mineralogical and Geochemical Characteristics of the Parnassos-Ghiona Bauxite Deposits, Greece. *J. Geochem. Explor.* **2007**, *93*, 67–77. [CrossRef]
60. Magendran, T.; Sanjeevi, S. A Study on the Potential of Satellite Image-Derived Hyperspectral Signatures to Assess the Grades of Iron Ore Deposits. *J. Geol. Soc. India* **2013**, *82*, 227–235. [CrossRef]

61. Kasmaeeyazdi, S.; Dinelli, E.; Braga, R. Mapping Co–Cr–Cu and Fe Occurrence in a Legacy Mining Waste Using Geochemistry and Satellite Imagery Analyses. *Appl. Sci.* **2022**, *12*, 1928. [CrossRef]
62. Nikolakopoulos, K.G.; Tsombos, P.I.; Skianis, G.A.; Vaiopoulos, D.A. EO-1 Hyperion and ALI Bands Simulation to Landat 7 ETM + Bands for Mineral Mapping in Milos Island. In Remote Sensing for Environmental Monitoring, GIS Applications, and Geology VIII, Proceedings of the SPIE Remote Sensing, Wales, UK, 15–18 September 2008; SPIE: Bellingham, WA, USA, 2008; Volume 7110.
63. Rockwell, B.W. *Comparative Mineral Mapping in the Colorado Mineral Belt Using AVIRIS and ASTER Remote Sensing Data Mauritania Minerals Project View Project*; U.S. Geological Survey: Reston, VA, USA, 2013. [CrossRef]
64. Cull, S.; Cravotta, C.A.; Klinges, J.G.; Weeks, C. Spectral Masking of Goethite in Abandoned Mine Drainage Systems: Implications for Mars. *Earth Planet. Sci. Lett.* **2014**, *403*, 217–224. [CrossRef]
65. Santos, D.; Cardoso-Fernandes, J.; Lima, A.; Teodoro, A.C. Assessing the Potential of PlanetScope Imagery for Iron Oxide Detection in Antimony Exploration. *Remote Sens.* **2025**, *17*, 2511. [CrossRef]

Disclaimer/Publisher's Note: The statements, opinions and data contained in all publications are solely those of the individual author(s) and contributor(s) and not of MDPI and/or the editor(s). MDPI and/or the editor(s) disclaim responsibility for any injury to people or property resulting from any ideas, methods, instructions or products referred to in the content.